Identification and Characterization of a Large Sample of Distant Active Dwarf Galaxies in XMM-SERVS

Fan Zou[1,2] , W. N. Brandt[1,2,3] , Qingling Ni[4] , Shifu Zhu[1,2] , David M. Alexander[5] , Franz E. Bauer[6,7,8,9] ,
Chien-Ting J. Chen[10,11] , Bin Luo[12,13] , Mouyuan Sun[14] , Cristian Vignali[15,16] , Fabio Vito[16] , Yongquan Xue[17,18] , and
Wei Yan[1,2]

[1] Department of Astronomy and Astrophysics, 525 Davey Laboratory, The Pennsylvania State University, University Park, PA 16802, USA; fuz64@psu.edu
[2] Institute for Gravitation and the Cosmos, The Pennsylvania State University, University Park, PA 16802, USA
[3] Department of Physics, 104 Davey Laboratory, The Pennsylvania State University, University Park, PA 16802, USA
[4] Max-Planck-Institut für extraterrestrische Physik (MPE), Gießenbachstraße 1, D-85748 Garching bei München, Germany
[5] Centre for Extragalactic Astronomy, Department of Physics, Durham University, South Road, Durham, DH1 3LE, UK
[6] Instituto de Astrofísica, Facultad de Física, Pontificia Universidad Católica de Chile, Campus San Joaquín, Avenida Vicuña Mackenna 7820436, 4860, Macul
Santiago, Chile
[7] Centro de Astroingeniería, Facultad de Física, Pontificia Universidad Católica de Chile, Campus San Joaquín, Avenida Vicuña Mackenna 7820436, 4860, Macul
Santiago, Chile
[8] Millennium Institute of Astrophysics, Nuncio Monseñor Sótero Sanz 100, of 104, Providencia, Santiago, Chile
[9] Space Science Institute, 4750 Walnut Street, Suite 205, Boulder, CO 80301, USA
[10] Science and Technology Institute, Universities Space Research Association, Huntsville, AL 35805, USA
[11] Astrophysics Office, NASA Marshall Space Flight Center, ST12, Huntsville, AL 35812, USA
[12] School of Astronomy and Space Science, Nanjing University, Nanjing, Jiangsu 210093, People's Republic of China
[13] Key Laboratory of Modern Astronomy and Astrophysics (Nanjing University), Ministry of Education, Nanjing 210093, People's Republic of China
[14] Department of Astronomy, Xiamen University, Xiamen, 361005, Fujian, People's Republic of China
[15] Dipartimento di Fisica e Astronomia "Augusto Righi," Alma Mater Studiorum, Università degli Studi di Bologna, Via Gobetti 93/2, I-40129 Bologna, Italy
[16] INAF—Osservatorio di Astrofisica e Scienza dello Spazio di Bologna, Via Gobetti 93/3, I-40129 Bologna, Italy
[17] CAS Key Laboratory for Research in Galaxies and Cosmology, Department of Astronomy, University of Science and Technology of China, Hefei 230026, People's
Republic of China
[18] School of Astronomy and Space Sciences, University of Science and Technology of China, Hefei 230026, People's Republic of China

Abstract

Active dwarf galaxies are important because they contribute to the evolution of dwarf galaxies and can reveal their hosted massive black holes. However, the sample size of such sources beyond the local universe is still highly limited. In this work, we search for active dwarf galaxies in the recently completed XMM-Spitzer Extragalactic Representative Volume Survey (XMM-SERVS). XMM-SERVS is currently the largest medium-depth X-ray survey covering $13\,\mathrm{deg}^2$ in three extragalactic fields, which all have well-characterized multiwavelength information. After considering several factors that may lead to misidentifications, we identify 73 active dwarf galaxies at $z < 1$, which constitutes the currently largest X-ray-selected sample beyond the local universe. Our sources are generally less obscured than predictions based on the massive-AGN (active galactic nucleus) X-ray luminosity function and have a low radio-excess fraction. We find that our sources reside in environments similar to those of inactive dwarf galaxies. We further quantify the accretion distribution of the dwarf-galaxy population after considering various selection effects and find that it decreases with X-ray luminosity, but redshift evolution cannot be statistically confirmed. Depending on how we define an AGN, the active fraction may or may not show a strong dependence on stellar mass. Their Eddington ratios and X-ray bolometric corrections significantly deviate from the expected relation, which is likely caused by several large underlying systematic biases when estimating the relevant parameters for dwarf galaxies. Throughout this work, we also highlight problems in reliably measuring photometric redshifts and overcoming strong selection effects for distant active dwarf galaxies.

Unified Astronomy Thesaurus concepts: Dwarf galaxies (416); Intermediate-mass black holes (816); X-ray active galactic nuclei (2035)

1. Introduction

Supermassive black holes (SMBHs) are known to be prevalent in massive galaxies and appear to be fundamentally linked to galaxy evolution (e.g., Kormendy & Ho 2013). However, our knowledge about dwarf galaxies, which are usually defined as galaxies with stellar masses ($M_\star$) comparable to or smaller than that of the Large Magellanic Cloud ($3 \times 10^9\,M_\odot$), and the massive black holes (MBHs; $\gtrsim 10^2\,M_\odot$,

i.e., more massive than stellar-mass BHs) residing in them (if present) is scarcer, primarily because they have lower luminosities and were thus difficult to detect in previous wide surveys. MBHs in dwarf galaxies may include intermediate-mass black holes (IMBHs; 10^2–$10^5\,M_\odot$, i.e., between stellar-mass BHs and SMBHs; e.g., Greene et al. 2020) and small SMBHs ($\approx 10^5$–$10^6\,M_\odot$). In principle, the term "MBHs" can include SMBHs, but the latter are explicitly named SMBHs instead of MBHs in most cases. We will thus use MBHs to refer to IMBHs and small SMBHs ($\approx 10^2$–$10^6\,M_\odot$) in the following text, as done in previous literature (e.g., Reines 2022). Note that this is simply a choice of terminology, and the exact BH mass (M_{BH}) is not the focus of this work.

Although challenging, understanding MBHs in dwarf galaxies is vital in several respects. First, MBHs may play important roles in dwarf-galaxy evolution (e.g., Penny et al. 2018; Barai & de Gouveia Dal Pino 2019; Koudmani et al. 2019; Manzano-King et al. 2019). Our current understanding of galaxy evolution is mostly based on massive galaxies, but dwarf galaxies are numerically more abundant and are essential for a holistic understanding of galaxy assembly (e.g., Calabrò et al. 2017) and for their contribution to the metal enrichment of the intergalactic medium and the missing baryon problem (e.g., Tumlinson et al. 2017). Especially, dwarf galaxies and their MBHs are becoming increasingly of interest as upcoming wide surveys are becoming sensitive enough to probe the low-mass regime. Second, MBHs may provide significant insights into the seeds of SMBHs. High-redshift seed MBHs have been involved in the explanation of SMBHs (e.g., Inayoshi et al. 2020 and references therein). It is currently impossible to directly probe the seeds at high redshifts, but some of them presumably did not grow much and eventually evolved into MBHs at lower redshifts (e.g., Mezcua 2017). Hence, MBHs in dwarf galaxies are important for understanding SMBH seeding scenarios (e.g., Burke et al. 2023). Third, MBHs are possible engines of tidal disruption events and also the primary targets of the next-generation gravitational wave detector, the Laser Interferometer Space Antenna.

Searches for MBHs in dwarf galaxies have flourished over the past decade. Other than the dynamical searches that are limited to nearby galaxies, evidence of the existence of MBHs is mainly from their active galactic nucleus (AGN) signals (e.g., Greene et al. 2020; Reines 2022). Similar to some traditional searching techniques for AGNs in massive galaxies, astronomers have mainly used optical spectra, X-ray observations, and radio observations to search for active dwarf galaxies (i.e., dwarf galaxies with AGN activity). Mid-infrared AGN selection, however, seems to face severe challenges for dwarf galaxies because of source confusion and strong star formation (SF) contamination (Mezcua et al. 2018; Lupi et al. 2020). Variability-based AGN selection of active dwarf galaxies can help identify sources missed by the optical spectroscopic method and is expected to be increasingly important in the upcoming decade as the Vera C. Rubin Observatory Legacy Survey of Space and Time (LSST) becomes available, though the variability method has not been well explored beyond the local universe and often faces selection biases that are hard to characterize (e.g., Baldassare et al. 2018, 2020b; Burke et al. 2022; Ward et al. 2022). Future surveys that are both deep and wide, such as LSST, will enable detailed studies of distant dwarf galaxies in the future (e.g., LSST Science Collaboration et al. 2009).

Systematic searches for active dwarf galaxies beyond the local universe had not begun until roughly a decade ago and are mainly driven by deep X-ray (Schramm et al. 2013; Mezcua et al. 2016; Pardo et al. 2016; Aird et al. 2018; Mezcua et al. 2018) and sometimes radio (Mezcua et al. 2019; Davis et al. 2022) observations. Population analyses of distant active dwarf galaxies beyond the local universe are still mainly limited by the number of known sources. The current largest sample is probably from the Cosmic Evolution Survey (COSMOS) field in Mezcua et al. (2018), which is based on the medium-depth Chandra COSMOS Legacy Survey (Civano et al. 2016) and contains 40 sources, 12 of which are above $z = 0.5$. Aird et al. (2018) also analyzed $\approx$40–50 Chandra-detected active dwarf galaxies compiled from several fields. However, as our analyses will reveal, these sources should only be considered as candidates because several measurement problems were not recognized, and the number of real active dwarf galaxies in these samples may be even smaller.

In this work, we search for active dwarf galaxies in a recently finished XMM-Newton Survey, the XMM-Spitzer Extragalactic Representative Volume Survey (XMM-SERVS; Chen et al. 2018; Ni et al. 2021). It includes a total of 5.4 Ms of flare-filtered XMM-Newton observations in three fields—Wide Chandra Deep Field-South (W-CDF-S; 4.6 deg^2), European Large Area Infrared Space Observatory Survey-S1 (ELAIS-S1; 3.2 deg^2), and XMM-Newton Large Scale Structure (XMM-LSS; 5.3 deg^2). The survey provides a roughly uniform 50 ks exposure across the fields, reaching a flux limit of $\approx 10^{-15}$–10^{-14} erg cm^{-2} s^{-1} in the 0.5–10 keV band, with more than 10,000 AGNs detected. This is currently the largest medium-depth X-ray survey and covers an area about 6 times larger than the Chandra COSMOS Legacy Survey, though XMM-SERVS is slightly shallower, with flux limits differing by $\approx$0.2–0.5 dex. Therefore, XMM-SERVS is expected to provide a larger sample of distant active dwarf galaxies than that in Mezcua et al. (2018). Similar to COSMOS, the three XMM-SERVS fields have extensive multiwavelength observations, which enable good source characterization (e.g., Zou et al. 2022; hereafter Z22). Furthermore, COSMOS and the three XMM-SERVS fields have been chosen as LSST Deep-Drilling Fields (DDFs) and also will be targeted by many other facilities, as summarized in Z22. The upcoming LSST DDF time-domain observations are expected to find many variability-selected active dwarf galaxies (e.g., Baldassare et al. 2018, 2020b; Burke et al. 2022, 2023), and thus our X-ray selections in the same fields will provide further insights in the LSST era.

This paper is structured as follows. Section 2 describes the data and our selection of active dwarf galaxies. Section 3 presents the population analyses of our sample and relevant discussions. Section 4 summarizes this work. We adopt a flat Lambda cold dark matter cosmology with $H_0 = 70$ km s^{-1} Mpc^{-1}, $\Omega_\Lambda = 0.7$, and $\Omega_M = 0.3$.

2. Data and Sample

Our active dwarf galaxies are selected from XMM-SERVS. As per Section 1, this survey has superb multiwavelength photometric data from the X-ray to radio. Furthermore, its optical-to-near-infrared photometry has been refined using a forced-photometry technique (Zou et al. 2021a; Nyland et al. 2023), which minimizes source confusion in low-resolution images, ensures consistency among different bands, and improves photometric redshifts (photo-zs). The redshifts have been compiled from several spectroscopic campaigns and, when spectroscopic redshifts (spec-zs) are unavailable, photo-zs presented in Chen et al. (2018 for XMM-LSS) and Zou et al. (2021b; for W-CDF-S and ELAIS-S1)[19] are used. The number of bands used in the photo-z estimations is around 10−15 down to an i-band magnitude of $\approx$24. Z22 further measured host-galaxy properties (e.g., $M_\star$ and SFR) in the regions with good multiwavelength coverage in the XMM-SERVS fields by

---

[19] Ni et al. (2021) derived photo-zs for broad-line AGNs to complement Zou et al. (2021b), but such sources will be excluded from our sample in Section 2.1.1.

Table 1
Sample Sizes

	Initial	Photo-z	$M_\star^{\rm gal}$	X-Ray Excess
W-CDF-S	105 (78 + 27)	34 (7 + 27)	26 (7 + 19)	22 (4 + 18)
ELAIS-S1	78 (59 + 19)	26 (7 + 19)	20 (7 + 13)	13 (3 + 10)
XMM-LSS	170 (123 + 47)	62 (15 + 47)	49 (15 + 34)	38 (12 + 26)
Total	353 (260 + 93)	122 (29 + 93)	95 (29 + 66)	73 (19 + 54)

Note. This table summarizes the sample sizes as the selection criteria are progressively applied. The parentheses list the numbers of photo-z sources + spec-z sources. The second column, "Initial," refers to the criterion in the first paragraph of Section 2.1. The third column, "Photo-z," records the sample sizes after applying the photo-z quality cut in Section 2.1.1. The fourth column, "$M_\star^{\rm gal}$," shows the sample sizes with the $M_\star^{\rm gal}$ cut in Section 2.1.2 added further. The fifth column, "X-Ray Excess," shows our final sample sizes after applying the criterion in Section 2.2. We note that most sources fail both the photo-z and $M_\star^{\rm gal}$ cuts, and the drastic decreases in the sample sizes from the second column to the third column would still exist when switching the sequence of the photo-z and $M_\star^{\rm gal}$ cuts.

fitting source spectral energy distributions (SEDs) covering the X-ray to far-infrared (FIR) using CIGALE (Yang et al. 2022), where the AGN emission has been appropriately considered. We refer readers to Z22 for more details on the SED fitting and the related validation and analyses. We limit our analyses to the footprints cataloged by Z22, i.e., covered by the VISTA Deep Extragalactic Observations survey (VIDEO; Jarvis et al. 2013) because quality multiwavelength data are essential for detecting and characterizing dwarf galaxies. The areas are slightly smaller (mainly for XMM-LSS) than the whole XMM-SERVS area, and they cover 4.6, 3.2, and 4.7 deg^2 in W-CDF-S, ELAIS-S1, and XMM-LSS, respectively.

2.1. Selection of X-Ray-detected Dwarf Galaxies

We select nonstellar X-ray sources with $M_\star < 3 \times 10^9 \, M_\odot$ as active dwarf-galaxy candidates, where $M_\star$ is from the AGN-template SED fitting in Z22. One may think of using a more conservative criterion with uncertainties included, such as $M_\star + 2{\rm Err}(M_\star) < 3 \times 10^9 M_\odot$, where ${\rm Err}(M_\star)$ is the uncertainty of $M_\star$. When adopting the cataloged errors in Z22 as ${\rm Err}(M_\star)$, most sources (86%) in our final sample would satisfy this criterion, and the largest $M_\star + 2{\rm Err}(M_\star)$ value would only be 0.3 dex above $3 \times 10^9 \, M_\odot$. Our ${\rm Err}(M_\star)$ is generally small, with a median value of 0.11 dex, and it is far from being the dominant uncertainty compared to other selection effects that will be discussed later. We thus still adopt the standard criterion of $M_\star < 3 \times 10^9 \, M_\odot$.

We also require the best-fit reduced chi-square (χ_r^2) of the SED fitting to be smaller than five to remove poor fits, as adopted in Z22. The χ_r^2 distribution peaks at ≈ 1 with a light high-χ_r^2 tail. Only 6% of sources are removed, and there are 353 sources left in total, including 105 sources in W-CDF-S, 78 sources in ELAIS-S1, and 170 sources in XMM-LSS. However, we found that these requirements are far from sufficient to ensure reliability, and we will further apply stricter cuts in the following subsections. We summarize our sample sizes after adding several criteria in Table 1.

2.1.1. Photo-z Reliability

Although the photo-zs in Chen et al. (2018) and Zou et al. (2021b) have been proven to be generally accurate, they are expected to be much less reliable for active dwarf galaxies. The problems are twofold, caused by both the dwarf nature and the active nature of our sources. First, the Balmer break in galaxy spectra is an important feature for measuring photo-zs, but it becomes weak as the stellar age and metallicity decrease (see, e.g., Figure 4 in Paulino-Afonso et al. 2020). Dwarf galaxies

generally have young light-weighted stellar ages (i.e., with recent SF) and low metallicities (e.g., Gallazzi et al. 2005); thus, the corresponding galaxy SEDs may be close to power-laws, causing strong challenges to their photo-z measurements. Second, AGN contributions were not considered when deriving photo-zs in Chen et al. (2018) and Zou et al. (2021b), but our sources may have considerable AGN contributions.

To illustrate this, we use the specific SFR (sSFR = SFR/$M_\star$) to represent the Balmer break and the best-fit fractional AGN contribution in the observed-frame 0.36–4.5 μm band, $f_{\rm AGN}(0.36$–$4.5 \, \mu{\rm m}; {\rm obs})$, to quantify the impact of the AGN emission on the photo-z estimations. We show sSFR and $f_{\rm AGN}(0.36$–$4.5 \, \mu{\rm m}; {\rm obs})$ versus Q_z, the photo-z quality indicator in Chen et al. (2018) and Zou et al. (2021b), in Figure 1 for all the X-ray sources in XMM-SERVS with spec-zs, color coded by $|\Delta z|/(1 + z) = |z_{\rm phot} - z_{\rm spec}|/(1 + z_{\rm spec})$. Q_z is an empirical parameter defined in Brammer et al. (2008) and combines several kinds of information—best-fit chi-square, confidence interval width, and the fraction of the total photo-z probability within a given redshift range. Small Q_z indicates high reliability. Sources with $|\Delta z|/(1 + z) \geqslant 0.15$ are catastrophic outliers and correspond to the darkest brown points in the figure. The figure indicates that Q_z is positively correlated with sSFR and $f_{\rm AGN}(0.36$–$4.5 \, \mu{\rm m}; {\rm obs})$, and $|\Delta z|/(1 + z)$ generally strongly increases with Q_z. Note that we found that $f_{\rm AGN}(0.36$–$4.5 \, \mu{\rm m}; {\rm obs})$ is much more strongly correlated with Q_z than for the more fundamental fractional AGN contribution in the IR, $f_{\rm AGN}({\rm IR})$, cataloged in Z22 because photo-zs were derived based on SEDs only limited to the observed-frame 0.36–4.5 μm. Most of our sources have large sSFR and/or $f_{\rm AGN}(0.36$–$4.5 \, \mu{\rm m}; {\rm obs})$ and are also catastrophic photo-z outliers. We found that sources (both the general XMM-SERVS sources and dwarfs) with $Q_z < 0.15$ have $|\Delta z|/(1 + z) < 0.15$ in nearly all the cases, and thus we empirically adopt $Q_z = 0.15$ as the threshold for reliable photo-z measurements for our sources. This threshold is stricter than the nominal high-quality photo-z threshold, $Q_z = 1$, in Chen et al. (2018) and Zou et al. (2021b). We further require the best-fit photo-z to be between its 68% lower and upper limits; otherwise, the photo-z probability distribution may have multiple peaks or be highly skewed.

For sources with significant characteristics that are similar to spectroscopic broad-line AGNs (e.g., with AGN-dominated SEDs), Ni et al. (2021) derived their photo-zs using a dedicated method different from that in Zou et al. (2021b), and nearly all of them have $Q_z > 1$ in Zou et al. (2021b). We are unable to calibrate these photo-zs from Ni et al. (2021) for our dwarf sample because only one of them has a spec-z after the $M_\star^{\rm gal}$ cut
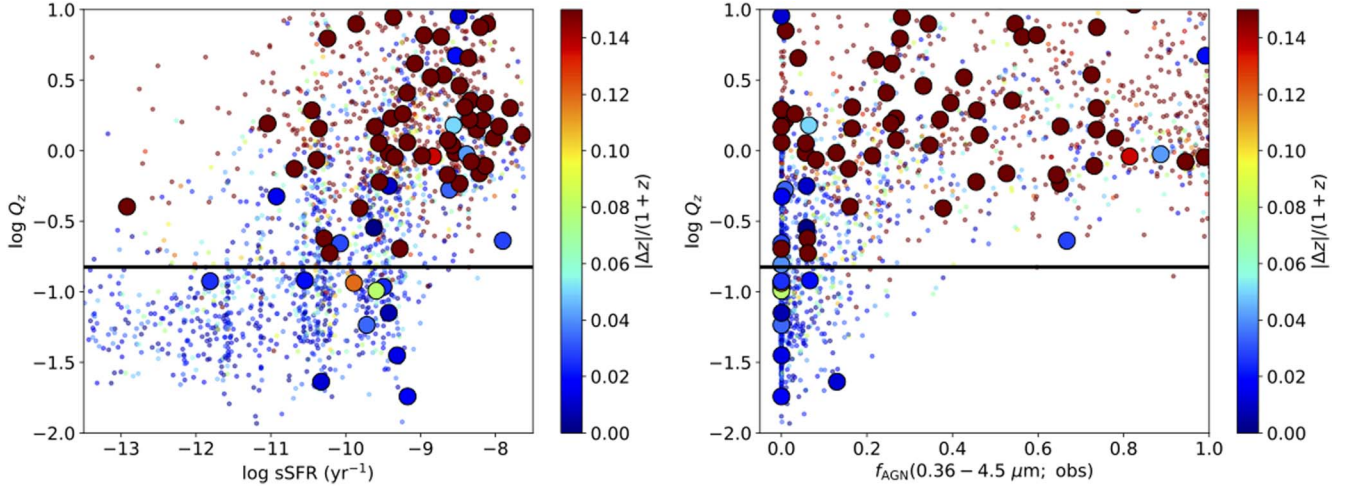
Figure 1. $\log Q_z$ vs. logsSFR (left) and $f_{\mathrm{AGN}}(0.36 - 4.5\ \mu m;\ \mathrm{obs})$ (right) for all the X-ray sources in XMM-SERVS with spec-zs, color coded by $|\Delta z|/(1 + z)$. Galaxies with cataloged $M_\star < 3 \times 10^9\ M_\odot$ are marked with large points. The horizontal black lines are $Q_z = 0.15$, our threshold for reliable photo-zs. Many of our photo-zs are unreliable because of high sSFR and $f_{\mathrm{AGN}}(0.36–4.5\ \mu m;\ \mathrm{obs})$.

(see Section 2.1.2 for more details) and turns out to have a photo-z inconsistent with its spec-z. Besides, the photo-zs and $M_\star$ of broad-line AGNs are generally expected to be less reliable. We hence further exclude these broad-line AGNs with photo-zs from Ni et al. (2021). Even if we include them without any photo-z quality cut, our final sample size would only increase by 9%.

The photo-z quality cut is only applied to those candidates without spec-zs and removes 231 sources. 122 sources are left, including 34, 26, and 62 sources in W-CDF-S, ELAIS-S1, and XMM-LSS, respectively. We show sources in the $f_{\mathrm{AGN}}(0.36\ \mu m;\ \mathrm{obs})-$sSFR plane in Figure 2. For sources without spec-zs, the quality cut only retains those with $\mathrm{sSFR} \lesssim 10^{-9}\ \mathrm{yr}^{-1}$ and $f_{\mathrm{AGN}}(0.36–4.5\ \mu m;\ \mathrm{obs}) \approx 0$. The sources with spec-$z$s, instead, are more scattered in Figure 2. This highlights the importance of obtaining deep spectroscopic observations in these fields; otherwise, the photo-z quality cut will exert strong selection effects on the active dwarf-galaxy sample. The cut also tends to remove high-redshift sources, which generally require higher $f_{\mathrm{AGN}}(0.36–4.5\ \mu m;\ \mathrm{obs})$ to be detectable in the X-ray and also have higher sSFR, as the star-forming galaxy main sequence (SFMS) increases with redshift. Although it is inevitable that sources with unreliable redshifts may have biased $f_{\mathrm{AGN}}(0.36–4.5\ \mu m;\ \mathrm{obs})$ and sSFR, which may undermine Figure 2, our adopted cut is independent of these two parameters.

We emphasize that the difficulty of deriving reliable photo-zs discussed in this section is not unique to our fields. We have checked the active dwarf-galaxy sample in Mezcua et al. (2018) in COSMOS and compared their spec-zs and photo-zs cataloged in Marchesi et al. (2016). 9/21 are catastrophic photo-z outliers, indicating that the same problem likely also exists in COSMOS. As far as we know, this problem has not been noted before, and thus extra caution should be taken when analyzing previous active dwarf galaxies with only photo-zs beyond the local universe.

It is unclear to us how to practically refine the COSMOS sample with photo-zs because the photo-z methodologies in COSMOS are technically different. We also found small systematic offsets between some COSMOS SED-fitting results (e.g., Laigle et al. 2016) and the results in Z22—their SFMSs may differ by $\approx 0.1-0.3$ dex, possibly because of their different
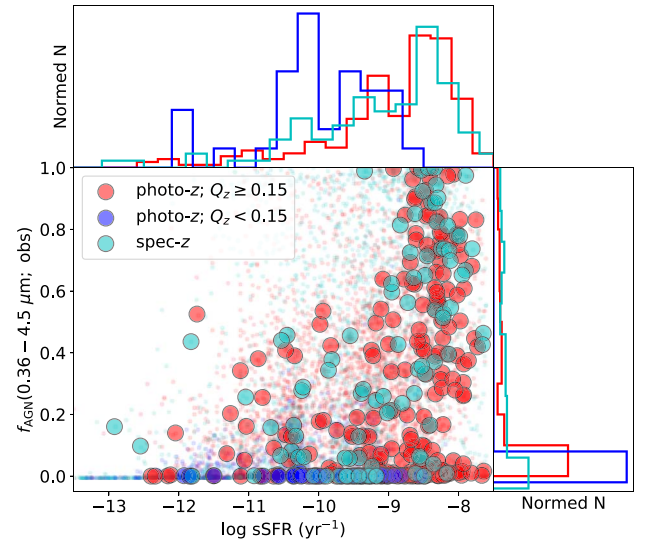

Figure 2. logsSFR vs. $f_{\mathrm{AGN}}(0.36–4.5\ \mu m;\ \mathrm{obs})$ for all the XMM-SERVS sources. Galaxies with cataloged $M_\star < 3 \times 10^9\ M_\odot$ are marked with large points. Distributions of logsSFR and $f_{\mathrm{AGN}}(0.36–4.5\ \mu m;\ \mathrm{obs})$ are shown in the top and right panels, respectively. Sources whose redshifts are photo-zs with $Q_z \gtrsim 0.15$ (i.e., the large red points) are removed from our sample. The photo-z quality cut only retains sources with small sSFR and near-zero $f_{\mathrm{AGN}}(0.36–4.5\ \mu m;\ \mathrm{obs})$.

SED-fitting methods. Such a systematic factor-of-two difference generally exists among different SED-fitting results. To ensure consistency, we do not include the COSMOS sample in our analyses. Besides, even if we do include the COSMOS sample, its sample size is too small to have a large impact on our results. As a rough estimation, the number of reliable active dwarf galaxies in Mezcua et al. (2018) should be $\lesssim 30$, while our final sample size (Section 2.3) in XMM-SERVS is 2–3 times larger.

2.1.2. $M_\star$ Reliability

We found that some best-fit SEDs are dominated by type 1 AGN emission, especially for sources with spec-zs $\gtrsim 1$. Figure 3 presents a high-redshift example and a bona fide active dwarf galaxy. For the high-redshift source, its galaxy
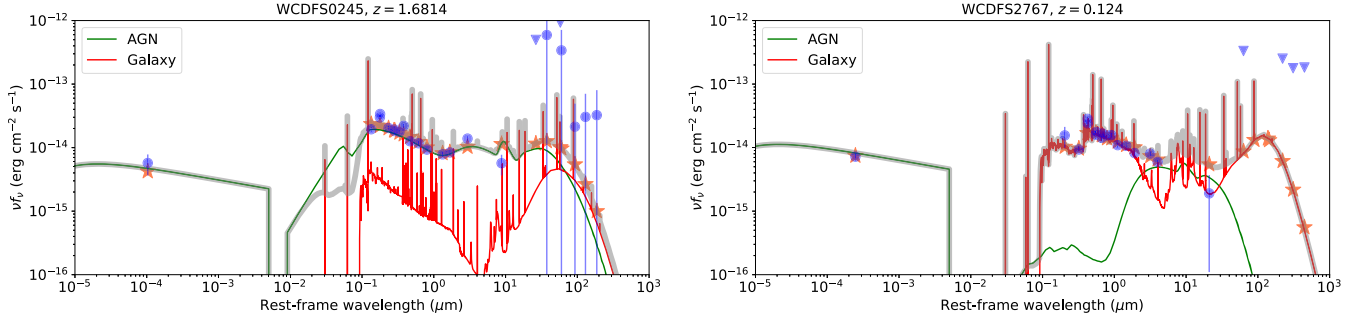
Figure 3. Example rest-frame SEDs from Z22 of high-redshift X-ray-detected dwarf galaxies with $M_\star < 3 \times 10^9 \, M_\odot$ (left) and bona fide active dwarf galaxies (right). The source XIDs and redshifts are listed as the panel titles. The blue points and downward triangles are the observed photometry and upper limits, respectively. The orange stars are the best-fit modeled photometry in the given bands, and the thick gray lines represent the best-fit models. The SEDs are decomposed into AGN components (green) and galaxy components (red). In contrast to the right panel, the AGN component in the left panel dominates the optical-to-NIR SED, and thus the host $M_\star$ cannot be measured reliably.
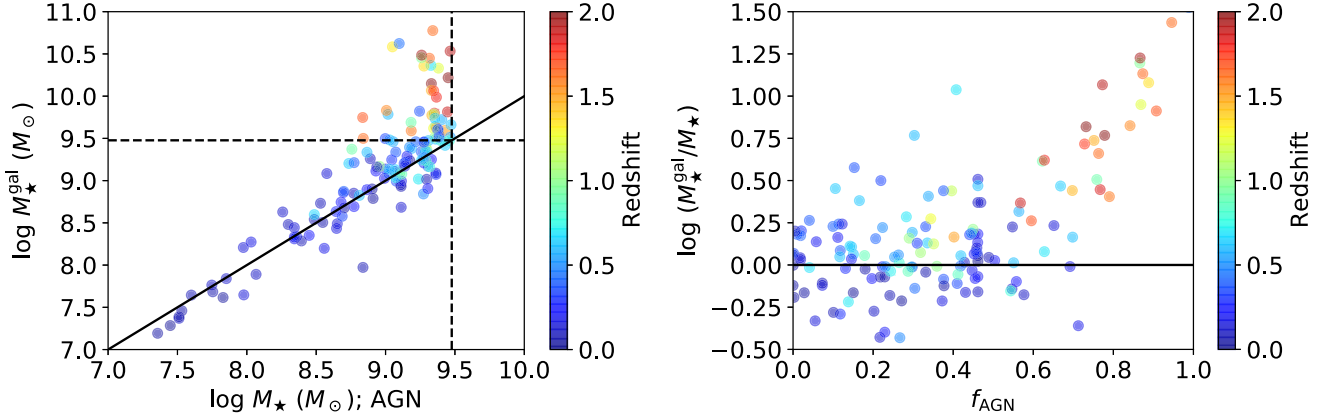

Figure 4. Left: comparison between $M_\star^{\mathrm{gal}}$ and the adopted AGN-template-based $M_\star$ values, color coded by redshift. The black solid line represents a one-to-one relationship, and the black-dashed lines are our adopted mass threshold ($3 \times 10^9 \, M_\odot$) for both $M_\star^{\mathrm{gal}}$ and $M_\star$. Sources above $M_\star^{\mathrm{gal}} = 3 \times 10^9 \, M_\odot$ are not considered. Right: difference between $M_\star^{\mathrm{gal}}$ and $M_\star$ vs. $f_{\mathrm{AGN}}(\mathrm{IR})$, color coded by the redshift. The black solid line represents zero difference. The difference between $M_\star^{\mathrm{gal}}$ and $M_\star$ generally increases with $f_{\mathrm{AGN}}(\mathrm{IR})$, and high-redshift sources tend to have larger $f_{\mathrm{AGN}}(\mathrm{IR})$ and often exceed the threshold of $M_\star^{\mathrm{gal}}$.

emission makes little contribution to its optical-to-NIR (near-infrared) SED. For such sources, the $M_\star$ measurements are usually unreliable, and the SED fitting may arbitrarily return small $M_\star$ values, which may range below $3 \times 10^9 \, M_\odot$, regardless of the real $M_\star$.

To quantify this effect, we first denote $M_\star^{\mathrm{gal}}$ as the fitted $M_\star$ based on normal-galaxy templates (i.e., without AGN components) in Z22. Since the total emission from both the AGN and galaxy components is assigned only to the galaxy when deriving $M_\star^{\mathrm{gal}}$, this parameter is expected to be close to the AGN-template-based $M_\star$ when the AGN contribution is small and gives a soft upper limit for the actual $M_\star$ when the AGN contribution is non-negligible. We compare $M_\star^{\mathrm{gal}}$ with the adopted AGN-template-based $M_\star$ for our candidates in the left panel of Figure 4, and high-z sources tend to have much larger $M_\star^{\mathrm{gal}}$ than the dwarf-galaxy $M_\star$ threshold. The right panel of Figure 4 shows the difference between the two $M_\star$ measurements versus $f_{\mathrm{AGN}}(\mathrm{IR})$ in Z22, where the difference increases with $f_{\mathrm{AGN}}(\mathrm{IR})$, as expected, and high-$z$ sources also generally have high-$f_{\mathrm{AGN}}(\mathrm{IR})$ values. These indicate that it is challenging to confirm the dwarf nature of high-z active dwarf-galaxy candidates because their strong AGN emission outshines their hosts. To avoid this SED issue, we remove 27 sources with $M_\star^{\mathrm{gal}} \geqslant 3 \times 10^9 \, M_\odot$, and this requirement provides a conservative dwarf-galaxy criterion. All of our candidates with $z > 1.1$ fail the $M_\star^{\mathrm{gal}}$ criterion, and 95 sources are left, including

26, 20, and 49 in W-CDF-S, ELAIS-S1, and XMM-LSS, respectively. Also note that all the photo-z sources surviving the photo-z quality cut in Section 2.1.1 pass the $M_\star^{\mathrm{gal}}$ cut, as expected.

The above $M_\star^{\mathrm{gal}}$ criterion only addresses the problem that the stellar emission may be outshined and thus *hidden* by the AGN emission. However, old stars can also be hidden by young stars, and neglecting such old stars may cause underestimations of $M_\star$, especially for starburst galaxies (e.g., Papovich et al. 2001). This is related to the adopted star formation history (SFH). The normal galaxy $M_\star^{\mathrm{gal}}$ in Z22 is based on delayed SFHs, which can provide good characterizations for general galaxies, whose main stellar populations are either young or old, but cannot describe the starburst case with both very young and old stellar populations. Fortunately, our sources are generally not starburst galaxies (see Figure 2), and only two sources in our final sample (see Section 2.3) have sSFR $> 10^{-8} \, \mathrm{yr}^{-1}$. More conservatively, we further check the $M_\star^{\mathrm{gal}}$ based on *bursting or quenching* (BQ) SFHs in Z22 (denoted as $M_\star^{\mathrm{bqgal}}$),[20] which allow the existence of an old stellar population besides a young population and thus generally return larger $M_\star$. Such $M_\star^{\mathrm{bqgal}}$ values should be even more conservative upper limits for the real $M_\star$, and we found that only 15% of our final sample would then have

---

[20] We adopt their BQ results based on their Table 3 instead of their cataloged results from their Table 6 because the latter are not run for most sources.

$M_\star^{\mathrm{bqgal}} > 3 \times 10^9\,M_\odot$. Only one source (XID=XMM02399), which also turns out to have interesting properties, exceeds $10^{10}\,M_\odot$, and we discuss this source in detail in Appendix B (see also Section 3.1). The normal-galaxy $M_\star^{\mathrm{gal}}$ criterion could be adjusted to the one based on $M_\star^{\mathrm{bqgal}}$. However, it should be noted that we are not really improving anything by changing SFHs, but instead trying to identify underlying plausible systematic uncertainties. It is well known that SED fitting has an inherent factor-of-2 uncertainty that can hardly be narrowed down (e.g., Conroy 2013; Leja et al. 2019; Pacifici et al. 2023; Z22) because of various factors, including the choice of SFH. Besides, AGN studies rarely adopt BQ SFHs or similar complex ones because of much heavier computational requirements and strong degeneracies with the AGN emission (e.g., see Section 4.5 of Z22), and thus adopting normal-galaxy SFHs ensures a general consistency with the literature. We thus still adopt the original normal-galaxy $M_\star^{\mathrm{gal}}$ criterion, but the inevitable uncertainty in $M_\star$ discussed in this paragraph should be kept in mind.

2.2. Selection of Active Dwarf Galaxies

We then assess if the detected X-rays are sufficiently bright to indicate the presence of AGNs residing in these dwarf galaxies. We directly compare their counts instead of fluxes for better accuracy. Due to the non-negligible point-spread function (PSF) size of XMM-Newton, nearby galaxies close to the dwarf of interest may also contribute to the observed emission. Therefore, the observed counts are from both the surrounding sources and the dwarf galaxies themselves.

For a given dwarf of interest, we select sources in Z22 within $1'$, a sufficiently large radius, around this dwarf as its nearby sources. If a nearby source is cataloged in XMM-SERVS, we directly adopt its observed counts as the contribution. For the others, some of them may be AGNs as well, and we select AGNs as those being identified as mid-IR or reliable SED AGNs in Section 3.2 of Z22 and adopt their expected X-ray emission as the predicted values through SED fitting in Section 3.2.2 of Z22. Note that these predictions are intrinsic X-ray emission before absorption by the intrinsic obscuration and thus may overestimate the fluxes. However, this is acceptable because we want to be conservative. These neighboring galaxies are assumed to be from the general galaxy population (i.e., not subpopulations with special properties such as our active dwarf galaxies), and thus their redshifts and galaxy properties should be reliable, as justified in detail in Chen et al. (2018), Zou et al. (2021b), and Z22.

For non-AGN normal galaxies, their X-ray emission is mainly from X-ray binaries (XRBs) and hot gas, where the hot gas emission mainly contributes in the soft X-rays. We estimate their X-ray fluxes following similar procedures as Basu-Zych et al. (2020). Note that we correct the $M_\star$ and SFR differences among the literature caused by different initial mass functions (IMFs) following Speagle et al. (2014) and Madau & Dickinson (2014):

$$M_\star^C = 0.94 M_\star^K = 0.58 M_\star^S, \tag{1}$$

$$\mathrm{SFR}^C = 0.94\,\mathrm{SFR}^K = 0.63\,\mathrm{SFR}^S, \tag{2}$$

where the superscripts "C," "K," and "S" represent the Chabrier (Chabrier 2003), Kroupa (Kroupa 2001), and Salpeter (Salpeter 1955) IMFs, respectively. The $M_\star$ and SFR differences from the Chabrier and Kroupa IMFs are generally negligible, but the Salpeter IMF can cause noticeable differences. We will always use the Chabrier IMF $M_\star$ and SFR, as adopted in Z22, in the following text.

We adopt the scaling relation in Lehmer et al. (2016) for the XRB emission, where the total XRB emission is further separated into the contributions from low-mass XRBs (LMXBs) and high-mass XRBs (HMXBs). The LMXB and HMXB emission scales with $M_\star$ and SFR, respectively. Their relation gives

$$\begin{aligned} L_{2-10\,\mathrm{keV}}^{\mathrm{XRB}} &= L_{2-10\,\mathrm{keV}}^{\mathrm{LMXB}} + L_{2-10\,\mathrm{keV}}^{\mathrm{HMXB}} \\ &= 10^{29.30}(1+z)^{2.19}M_\star^K + 10^{39.40}(1+z)^{1.02}\mathrm{SFR}^K, \end{aligned} \tag{3}$$

where the luminosity, $M_\star$, and SFR are in erg s^{-1}, $M_\odot$, and $M_\odot\,\mathrm{yr}^{-1}$, respectively. We adopt a power law with a photon index of $\Gamma = 1.8$ as the XRB spectrum.

For the hot gas emission, mass-dominated galaxies and galaxies dominated by SF have different scaling relations, where the hot gas emission from the former and the latter mainly scales with $M_\star$ and SFR, respectively. Following Basu-Zych et al. (2020), we regard a galaxy as mass dominated or SF dominated if its sSFR is smaller or larger than $10^{-10.1}\,\mathrm{yr}^{-1}$, respectively. We adopt the scaling relation in Kim & Fabbiano (2015) for mass-dominated galaxies:

$$\log(L_{0.3-8\,\mathrm{keV}}^{\mathrm{gas}}/10^{40}\,\mathrm{erg\,s}^{-1}) = 2.98\log(L_K/10^{11}L_{K\odot}) - 0.25, \tag{4}$$

where L_K is the K-band luminosity. We further use $M_\star/M_\odot = 0.66 L_K/L_{K\odot}$ (Lehmer et al. 2014) to convert the above luminosity scaling relation to an $M_\star$ scaling relation. Following Kim & Fabbiano (2015), we adopt the corresponding hot gas spectrum as an `apec` model with the gas temperature kT set by the following equation:

$$\log(L_{0.3-8\,\mathrm{keV}}^{\mathrm{gas}}/10^{40}\,\mathrm{erg\,s}^{-1}) = 5.39\log(kT/0.5\,\mathrm{keV}) + 0.16. \tag{5}$$

For SF-dominated galaxies, we adopt the scaling relation in Mineo et al. (2012):

$$L_{0.5-2\,\mathrm{keV}}^{\mathrm{gas}} = 8.3 \times 10^{38}\mathrm{SFR}^S. \tag{6}$$

The corresponding spectrum is set to a `mekal` model with $kT = 0.5$ keV.

We follow the same procedures as above to estimate the galaxy emission from the dwarf targets themselves. The above scaling relations may underestimate the galaxy X-ray emission because dwarf galaxies generally have low metallicities and young ages (e.g., Gallazzi et al. 2005), which both elevate the LMXB and HMXB emission (e.g., Fragos et al. 2013; Prestwich et al. 2013; Lehmer et al. 2021). However, this almost does not cause any problem because the resulting expected galaxy emission from the dwarf targets is one order of magnitude smaller than that from their nearby sources. For example, we have tried using the metallicity- and age-dependent scaling relations in Fragos et al. (2013) and Lehmer et al. (2021), where we estimate metallicities based on the fundamental metallicity relation in Curti et al. (2020) and stellar ages from the best-fit SFHs in Z22, and the resulting final sample size in Section 2.3 only decreases by at most one.

Given the luminosity and the appropriate spectral models above, we can calculate the total expected X-ray flux in any desired X-ray band by applying corresponding K corrections using `sherpa` (Freeman et al. 2001; Doe et al. 2007). We then convert the expected flux to the expected counts in each camera (EPIC MOS1, MOS2, and PN) by multiplying the ratios between the cataloged net counts in each camera and the flux of the target of interest in the XMM-SERVS catalogs. These expected counts need to be converted to those in a given source aperture of the target by multiplying by the enclosed energy fraction (EEF) within the target aperture, as discussed in the following text. Then, the expected counts within the target aperture are summed over all the cameras.

We adopt the target aperture as 3×3 pixels (i.e., $12'' \times 12''$) around the dwarf of interest. The EEF is the integration of the PSF within the aperture, denoted as $\mathrm{EEF}(r, \theta)$, where r is the separation between the nearby source and the target, and θ represents all the other parameters determining this system. We then apply appropriate weightings on θ and further eliminate θ: $\mathrm{EEF}(r) = E_\theta\{\mathrm{EEF}(r, \theta)\}$ and $\sigma^2_{\mathrm{EEF}}(r) = \mathrm{Var}_\theta\{\mathrm{EEF}(r, \theta)\}$. $\mathrm{EEF}(r)$ is used to convert the total expected counts from nearby sources to those in the target aperture in each camera and in each band, and $\sigma_{\mathrm{EEF}}(r)$ is the uncertainty of $\mathrm{EEF}(r)$, mainly driven by the variation of the PSF shape.

We adopt the parameterization in Read et al. (2011) for the PSF shape, in which the PSF is mainly described as an elliptical King profile plus an elliptical Gaussian core, and the corresponding parameters are stored in XMM-Newton Current Calibration Files. θ includes the relative angles of the PSF and the target aperture and parameters determining the PSF shape. For the angle parameters, their weights are flat. The PSF-shape parameters mainly include the photon energy and off-axis angle; we use the observed spectrum (i.e., after convolution with typical XMM-Newton response files) of a power law with a photon index of 1.4 as the photon-energy weight, and the weight of the off-axis angle is the angle itself.

We then compare the observed counts within the target aperture (C_{obs}) with the non-AGN prediction (i.e., the dwarf target is not an AGN). The relevant distributions are

$$C_{\mathrm{obs}}|C_{\mathrm{non-AGN}} \sim \mathrm{Poi}(B + C_{\mathrm{non-AGN}} + C_{\mathrm{AGN}}), \qquad (7)$$

$$C_{\mathrm{non-AGN}} \sim N_+(C_{\mathrm{pred}}, \sigma^2_{\mathrm{pred}}), \qquad (8)$$

where B is the expected background counts from the background maps, $C_{\mathrm{non-AGN}}$ is the expected counts from nearby sources and the galaxy emission of the target, C_{AGN} is the expected AGN counts from the target, C_{pred} is our predicted value for $C_{\mathrm{non-AGN}}$, σ_{pred} is the uncertainty of C_{pred}, and N_+ denotes a normal distribution truncated at 0. σ_{pred} includes σ_{EEF} the uncertainty of the expected fluxes, and we estimate the latter by propagating the uncertainties of $M_\star$ and SFR and adding 0.3 dex in quadrature for each involved galaxy to account for the typical scatters of the scaling relationships used previously. Strictly speaking, B partially overlaps with $C_{\mathrm{non-AGN}}$ because both include the average unresolved source emission, but this component is generally much smaller than B and thus does not cause noticeable problems even when double counted.
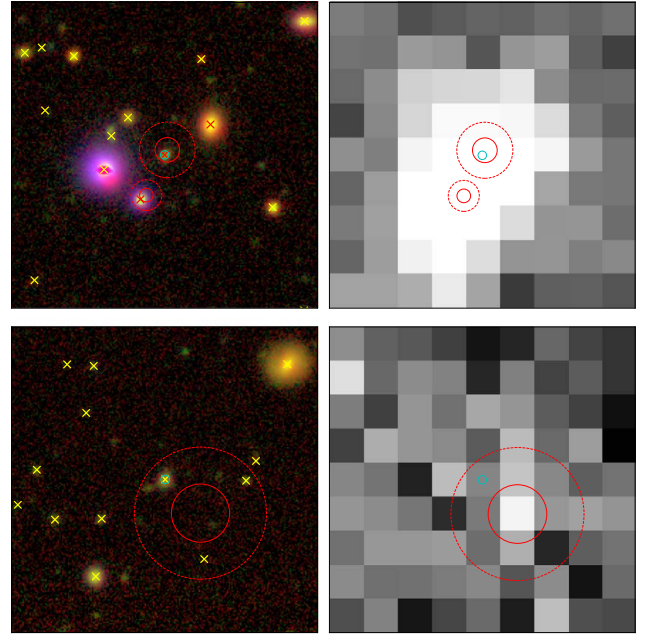

Figure 5. The optical (left) and XMM-Newton 0.2–12 keV (right) images of example sources failing the X-ray excess criterion. The top panels are for XID = WCDFS4029, and the bottom ones are for XID = WCDFS3998. The three-color optical images are generated from g-band (blue), i-band (green), and z-band (red) images from Ni et al. (2019; top). The red and yellow crosses mark AGNs and non-AGNs in Z22, respectively. The cyan circles are centered at the dwarf targets with radii of $0.5''$. The red solid and dashed circles represent 68% and 99.73% X-ray positional uncertainties, respectively, for the X-ray sources.

We then test the null hypothesis that $C_{\mathrm{AGN}} = 0$. From the above distributions, the p-value of the hypothesis test is

$$p - \mathrm{value} = \sqrt{\frac{2}{\pi}}$$
$$\times \frac{\int_0^{+\infty} P_{\mathrm{IG}}(C_{\mathrm{obs}}, B + x)\exp\left(-\frac{(x - C_{\mathrm{pred}})^2}{2\sigma^2_{\mathrm{pred}}}\right)dx}{\sigma_{\mathrm{pred}}\left[\mathrm{erf}\left(\frac{C_{\mathrm{pred}}}{\sqrt{2}\,\sigma_{\mathrm{pred}}}\right) + 1\right]}, \qquad (9)$$

where P_{IG} is the regularized lower incomplete gamma function. To mitigate the effects of obscuration, we choose the comparison band as follows. For sources detected in the hard band (HB), the comparison band is the HB; for sources undetected in the HB but detected in the full band (FB), the comparison band is the FB; for the remaining sources that are only detected in the soft band (SB), the comparison band is the SB. For W-CDF-S and ELAIS-S1, the SB, HB, and FB energy ranges are 0.2–2, 2–12, and 0.2–12 keV, respectively (Ni et al. 2021); while for XMM-LSS, the energy ranges are 0.5–2, 2–10, and 0.5–10 keV (Chen et al. 2018). We regard a source to be an active dwarf galaxy if its p-value is smaller than 0.01. This removes 21 sources and leaves 73 sources, including 22, 13, and 38 sources in W-CDF-S, ELAIS-S1, and XMM-LSS, respectively. We found that these hypothesis test results are not sensitive to σ_{pred}, and only three more sources are added even if we set $\sigma_{\mathrm{pred}} = 0$. This also indicates that it generally does not matter even if $C_{\mathrm{non-AGN}}$ does not strictly follow a truncated normal distribution as assumed.

Table 2
Source Catalog in W-CDF-S

XID	Tractor ID	R.A. (deg)	Decl. (deg)	z	z Type	$\log L_{X, obs}$ (erg s^{-1})	logSFR ($M_\odot$ yr^{-1})	$\log M_\star$ ($M_\odot$)	$\log M_\star^{gal}$ ($M_\odot$)	$\log M_\star^{bqgal}$ ($M_\odot$)
(1)	(2)	(3)	(4)	(5)	(6)	(7)	(8)	(9)	(10)	(11)
WCDFS0162	255877	51.905781	−28.958321	0.116	zphot	41.29	−1.48	8.89	9.26	8.91
WCDFS0217	364633	51.984135	−28.414293	0.123	zspec	41.36	−1.47	7.51	7.37	7.57
WCDFS0761	645301	51.833397	−27.244995	0.044	zspec	40.45	−0.70	9.18	9.24	9.18
WCDFS0986	453469	52.293705	−28.119442	0.150	zspec	41.28	−2.39	8.65	8.49	8.64
WCDFS1018	395902	52.600765	−28.227808	0.705	zspec	42.65	0.76	9.24	9.02	9.72
WCDFS1340	288812	52.637676	−28.778755	0.127	zspec	41.39	−1.01	7.85	7.84	8.13
WCDFS1346	265349	52.805256	−28.906603	0.645	zspec	43.21	0.04	8.74	9.20	9.30
WCDFS1355	352132	52.682285	−28.614000	0.916	zspec	42.89	0.51	8.76	9.37	9.63
WCDFS1394	350692	52.803371	−28.478706	0.042	zspec	40.88	−1.56	7.83	7.62	8.03
WCDFS1417	385839	52.793171	−28.373316	0.344	zspec	42.89	0.07	8.69	8.58	8.46
WCDFS1440	388690	52.752987	−28.272453	0.079	zspec	40.72	−2.99	8.84	7.97	8.33
WCDFS1459	402544	52.739395	−28.202730	0.111	zspec	40.91	−2.62	8.07	7.89	7.93
WCDFS1770	321314	53.202751	−28.624237	0.140	zspec	41.50	−0.70	9.11	8.68	9.06
WCDFS2044	504127	53.058399	−27.850225	0.122	zspec	42.02	−3.56	9.36	9.09	9.25
WCDFS2140	579203	53.082249	−27.483568	0.094	zphot	41.02	−3.18	8.30	8.48	8.30
WCDFS2759	76747	53.763737	−28.118191	0.364	zspec	42.66	0.24	9.08	8.99	9.24
WCDFS2767	50433	53.756840	−28.367943	0.124	zspec	41.55	−1.68	7.75	7.76	7.80
WCDFS2903	135853	53.713116	−27.707296	0.210	zspec	41.73	−0.48	8.70	8.86	8.78
WCDFS3040	14452	54.146523	−28.566229	0.156	zspec	41.35	−0.36	7.98	7.65	7.82
WCDFS3049	24383	54.123714	−28.513514	0.201	zspec	41.63	−0.24	9.00	9.14	8.93
WCDFS3606	663441	52.205837	−27.084970	0.116	zphot	41.04	−0.97	9.11	8.95	8.91
WCDFS4044	190734	53.735924	−27.263348	0.232	zphot	42.96	−1.44	8.93	9.11	9.06

Note. This table is sorted in ascending order as (1) XID, the XMM-SERVS source ID in Ni et al. (2021). (2) The source ID in Z22. (3) and (4) J2000 coordinates. (5) Redshift. (6) Redshift type. "zspec" and "zphot" indicate that the redshifts are spectroscopic and photometric redshifts, respectively. (7) Observed 2–10 keV luminosity. (8) and (9) AGN-template-based $M_\star$ and SFR in Z22. (10) and (11) normal-galaxy and BQ-galaxy template-based $M_\star$ in Z22, respectively.

Figure 5 presents optical and XMM-Newton images for two example sources that are removed, where the optical and XMM-Newton images have been aligned using the repro-ject package (Robitaille et al. 2020), and the optical image is from Ni et al. (2019). In the top panels of Figure 5 (XID = WCDFS4029), two additional AGNs are found to lie close to the dwarf galaxy, one of which is also included in the XMM-SERVS catalogs. This dwarf is clearly contaminated by the nearby AGNs and can hardly be cleaned reliably. In the bottom panels of Figure 5 (XID = WCDFS3998), the observed X-ray emission is not sufficiently strong. Therefore, the relatively larger PSF size of XMM-Newton compared to Chandra leads to source confusion and further complexity; due to the same reason, we lack the information on whether the X-ray emission is from the center or the outskirts of the host galaxy and thus can hardly exclude contamination from ultraluminous X-ray sources (ULXs). Some of these sources can reach a high L_X of 10^{42} erg s^{-1} (e.g., Farrell et al. 2009), though such cases are rare. Nevertheless, Mezcua et al. (2018) showed that, in COSMOS, the fraction of their active dwarf galaxies whose X-ray emission is actually from ULXs is generally limited ($\lesssim 15\%$), and similar conclusions are also drawn in Birchall et al. (2020) for nearby active dwarf galaxies selected through XMM-Newton. Thus, we expect that our sample also has limited ULX contamination.

2.3. Resulting Final Sample

The 73 sources remaining in Section 2.2 constitute our final active dwarf-galaxy sample. 54 of them (74%) have spectroscopic redshifts. The evolution of our sample sizes with selection criteria is summarized in Table 1. We summarize the

basic properties of our final sample in Tables 2–4 for W-CDF-S, ELAIS-S1, and XMM-LSS, respectively.

We present our sources in the $z - L_{X, obs}$, where $L_{X, obs}$ is the observed 2–10 keV luminosity, and $M_\star - L_{X, obs}$ planes in Figure 6. Table 1 and Figure 6 show that only a small fraction of sources can be retained in the final sample, highlighting the challenge of reliably searching for active dwarf galaxies beyond the local universe. Especially, high-redshift sources in the initial sample are less likely to be reliable, and they mainly fail the photo-z quality and $M_\star^{gal}$ cuts. We reiterate that our overall selection criteria are designed to be conservative, and it is possible that some of our excluded objects are real active dwarf galaxies, though this is challenging to pin down further, given our current data.

We have inspected their X-ray and optical images and did not find any apparent issues. We have also checked the matching between the XMM-SERVS catalogs and optical-to-IR catalogs. For W-CDF-S and ELAIS-S1, Ni et al. (2021) presented the false-matching rate as a function of a parameter, p_{any}. Our final sample has a mean p_{any} of 0.87 and 0.82 for W-CDF-S and ELAIS-S1, respectively, which corresponds to a false rate of ≈3% (see Figure 19 in Ni et al. 2021). For XMM-LSS, our mean matching reliability is 96%. Therefore, our final sample should have good matching reliability, and the expected mismatch rate is ≈3%, corresponding to ≈3 mismatched sources.

As a representative example, one of our sources (XID = WCDFS2044, R.A. = 03:32:14.02, decl. = −27:51:00.8, and spec-z = 0.122) resides in both the smaller Chandra Deep Field-South (CDF-S; Luo et al. 2017) and Hubble Legacy Fields GOODS-South (Illingworth et al. 2016; Whitaker et al. 2019) and thus has deeper and higher

Table 3
Source Catalog in ELAIS-S1

XID	Tractor ID	R.A. (deg)	Decl. (deg)	z	z Type	$\log L_{X,\,obs}$ (erg s^{-1})	logSFR ($M_\odot$ yr^{-1})	$\log M_\star$ ($M_\odot$)	$\log M_\star^{gal}$ ($M_\odot$)	$\log M_\star^{bqgal}$ ($M_\odot$)
(1)	(2)	(3)	(4)	(5)	(6)	(7)	(8)	(9)	(10)	(11)
ES0552	644246924653	9.443832	−43.783956	0.198	zspec	41.77	−2.05	8.34	8.31	8.30
ES0598	644246876754	8.917671	−43.935414	0.802	zspec	42.94	0.90	9.46	9.47	9.51
ES0618	644246961129	8.932128	−43.675953	0.078	zspec	40.52	−1.80	7.75	7.68	7.75
ES0695	644246995151	8.630936	−43.587412	0.052	zspec	40.58	−1.58	8.90	8.90	8.79
ES0875	644247085422	9.254822	−43.304044	0.220	zspec	42.31	−0.91	8.45	8.35	8.40
ES0904	644247097403	9.187931	−43.266448	0.058	zspec	40.53	−2.35	7.51	7.39	7.54
ES0922	644247059777	8.834723	−43.381866	0.627	zspec	43.01	1.12	9.29	9.34	9.23
ES1525	644246565825	10.076456	−44.636604	0.182	zspec	41.37	−1.26	9.11	8.99	9.09
ES1692	644246507665	9.727813	−44.838687	0.138	zphot	41.49	−0.57	9.07	9.11	9.00
ES1906	644246984907	9.495692	−43.606902	0.665	zspec	42.61	0.68	8.49	8.60	8.90
ES2302	644247133625	9.481544	−43.158952	0.186	zspec	41.85	−2.11	8.34	8.33	8.36
ES2367	644246584145	9.235555	−44.577481	0.196	zphot	41.32	−0.94	9.28	9.21	9.28
ES2468	644246664997	9.588642	−44.334487	0.105	zphot	40.57	−2.04	8.77	8.85	8.78

Note. Same as Table 2, but for ELAIS-S1.

angular-resolution Chandra and Hubble observations. We found apparent Chandra and Hubble counterparts of this source and plot its Hubble image in Figure 7. Its Hubble morphology has a Sérsic index of 4.2 and a half-light radius of 0.6 kpc (van der Wel et al. 2012), supporting its SED-fitting results in Z22 that WCDFS2044 is a quiescent dwarf galaxy ($M_\star = 2.3 \times 10^9\,M_\odot$ and SFR $= 2.8 \times 10^{-4}\,M_\odot$ yr^{-1}).

3. Analyses and Results

We further investigate several properties of our selected sample in this section. Section 3.1 analyzes X-ray hardness ratios (HRs) and obscuration. Section 3.2 presents the radio properties of our sources. Section 3.3 presents the cosmic environments. Section 3.4 derives the accretion distribution and active fraction of the dwarf-galaxy population. Section 3.5 discusses AGN bolometric luminosities, BH masses, and Eddington ratios of our sample.

3.1. HRs

The median FB net source counts of our sources is 122, insufficient for detailed X-ray spectral fitting. We thus analyze their HRs for simplicity to probe their spectral shapes. HR is defined as $(\lambda_H - \lambda_S)/(\lambda_H + \lambda_S)$, where λ_S and λ_H are the SB and HB source count rates, respectively. The cataloged XMM-SERVS HRs are only reliable mainly for sources detected in both the SB and HB, but many of our sources are only detected in the SB because the SB has higher sensitivity. Therefore, we recalculate the HRs of our sources and, to be consistent, all the XMM-SERVS sources for comparison.

The classical method of estimating the net count rate by directly subtracting the background fails for undetected bands, and thus we adopt a Bayesian method to correctly account for the Poisson nature. We follow the framework in Park et al. (2006) but revise the mathematical and algorithmic implementations, the details of which are presented in Appendix A. For each source, we obtain its X-ray image counts within 5×5 pixels (i.e., $20'' \times 20''$) and exposure time, and the expected background intensity is from background maps. The EEF within this given aperture is further absorbed into the exposure time for aperture correction. These are then utilized in our calculations in Appendix A to return posterior cumulative

distribution functions (CDFs) of HR, where we set the prior parameters as $\psi_{S1} = \psi_{H1} = 1$ and $\psi_{S2} = \psi_{H2} = 0$ (see Equation (A2) for their definitions). We adopt the HR as the 50th percentile of the CDF and the associated 1σ uncertainty range as the 16th–84th percentiles.

We present our sources in the $z-$HR plane in Figure 8, together with the expected $z-$HR curves for redshifted absorbed power-law models with photon indices between 1.4 and 2.6 and the Galactic absorption included. The curves are calculated using the Portable Interactive Multi-Mission Simulator (PIMMS).[21] For a given spectral model, we obtain the corresponding expected total net count rate in a given camera (EPIC PN, MOS1, and MOS2) and a given band, and the predicted HR is calculated as follows:

$$\mathrm{HR} = \frac{\sum_j (x_{H,j}\hat{\lambda}_{H,j}^{\mathrm{tot}} - x_{S,j}\hat{\lambda}_{S,j}^{\mathrm{tot}})}{\sum_j (x_{H,j}\hat{\lambda}_{H,j}^{\mathrm{tot}} + x_{S,j}\hat{\lambda}_{S,j}^{\mathrm{tot}})}, \qquad (10)$$

$$x_{S,j} = \mathrm{median}\{t_{\mathrm{exp},j}(\mathrm{SB})/t_{\mathrm{exp}}(\mathrm{SB})\}, \qquad (11)$$

$$x_{H,j} = \mathrm{median}\{t_{\mathrm{exp},j}(\mathrm{HB})/t_{\mathrm{exp}}(\mathrm{HB})\}, \qquad (12)$$

where $j \in \{\mathrm{PN, MOS1, MOS2}\}$, $t_{\mathrm{exp,\,j}}$ is from the single-camera exposure maps across our fields, t_{exp} is from the camera-merged exposure maps, and $\hat{\lambda}_{\bullet,i}^{\mathrm{tot}}$ is the PIMMS-predicted single-camera count rate. Note that it is still appropriate to calculate spectral shapes using photoelectric absorption up to $N_{\mathrm{H}} = 10^{23}\,\mathrm{cm}^{-2}$. The "reflection" component would only be prominent at much higher N_{H} ($>10^{24}\,\mathrm{cm}^{-2}$). Although the Compton-scattering losses out of the line of sight may become non-negligible at $N_{\mathrm{H}} \gtrsim 10^{23}\,\mathrm{cm}^{-2}$, this effect is nearly energy-independent at the XMM-Newton energy coverage and thus does not change the overall spectral shape. For example, Figure 5 in Li et al. (2019) can serve as a clear illustration—when only using the photoelectric absorption, the inferred N_{H} (i.e., the spectral shape) would not be biased up to $N_{\mathrm{H}} = 10^{24}\,\mathrm{cm}^{-2}$, but only the intrinsic emission (i.e., the spectral normalization) would be underestimated.

---

[21] https://heasarc.gsfc.nasa.gov/docs/software/tools/pimms.html

Table 4
Source Catalog in XMM-LSS

XID	Tractor ID	R.A. (deg)	Decl. (deg)	z	z Type	$\log L_{X,\,obs}$ (erg s^{-1})	$\log$SFR ($M_\odot$ yr^{-1})	$\log M_\star$ ($M_\odot$)	$\log M_\star^{gal}$ ($M_\odot$)	$\log M_\star^{bgal}$ ($M_\odot$)
(1)	(2)	(3)	(4)	(5)	(6)	(7)	(8)	(9)	(10)	(11)
XMM00235	846032	34.335213	−5.480953	0.018	zspec	40.18	−1.60	6.89	6.91	7.00
XMM00275	1064101	34.351822	−4.682919	0.621	zspec	42.76	0.66	9.30	9.34	9.55
XMM00309	1197673	34.367554	−4.229480	0.127	zphot	41.17	−2.04	8.26	8.63	8.41
XMM00310	1049050	34.368221	−4.717017	0.067	zspec	41.00	−3.85	8.70	8.68	8.65
XMM00557	1047971	34.482452	−4.736839	0.104	zspec	41.86	−1.29	8.94	9.16	8.85
XMM00569	959133	34.487633	−5.063463	0.240	zspec	42.43	−0.68	8.87	8.89	9.11
XMM00637	1182069	34.520947	−4.241128	0.390	zspec	42.71	0.57	8.77	9.21	9.50
XMM00768	1154153	34.597561	−4.383302	0.564	zspec	42.74	0.92	9.05	9.46	9.79
XMM00795	1197492	34.613106	−4.230209	0.050	zspec	40.25	−2.25	7.36	7.19	7.38
XMM00838	1057468	34.640095	−4.683757	0.403	zphot	41.95	−0.55	8.70	8.87	8.71
XMM00852	824637	34.644726	−5.551417	0.359	zspec	42.71	−0.04	9.13	9.20	9.08
XMM00893	1061574	34.671246	−4.711613	0.500	zspec	42.31	−0.40	9.02	9.08	8.97
XMM00929	1198658	34.688000	−4.194396	0.629	zspec	43.29	0.68	9.03	9.13	9.36
XMM00937	1158612	34.692986	−4.330591	0.405	zspec	42.74	0.74	9.22	9.46	9.39
XMM01271	1094414	34.872738	−4.567514	0.294	zspec	42.63	0.18	9.36	9.07	9.58
XMM01487	537544	34.993084	−5.055025	0.094	zphot	40.35	−1.52	8.53	8.73	8.57
XMM01643	618315	35.091015	−4.655634	0.285	zspec	42.03	−0.05	8.36	8.34	8.66
XMM01671	693786	35.107349	−4.309465	0.645	zspec	42.74	0.70	9.43	9.42	9.85
XMM01843	530442	35.193939	−5.092589	0.270	zspec	42.45	−0.38	8.64	8.63	8.67
XMM01944	694600	35.253357	−4.305611	0.492	zspec	43.06	0.32	9.27	8.84	9.48
XMM02309	483035	35.436298	−5.421105	0.093	zspec	40.86	−1.96	8.39	8.29	8.43
XMM02399	744798	35.485558	−4.132769	0.615	zspec	43.66	1.65	9.31	9.47	10.46
XMM02438	538356	35.513119	−5.053028	0.255	zspec	42.39	−1.00	9.33	9.25	9.40
XMM02611	517637	35.609409	−5.172750	0.062	zphot	40.58	−1.88	8.91	8.79	8.75
XMM02667	765953	35.634304	−4.296326	0.033	zspec	40.58	−1.63	7.45	7.28	7.52
XMM02884	741519	35.763706	−4.090158	0.872	zphot	43.59	0.30	9.12	9.08	9.14
XMM03004	480648	35.825909	−5.344553	0.082	zspec	41.44	−4.57	9.30	9.02	9.21
XMM03169	590232	35.912758	−4.797773	0.694	zphot	42.70	0.72	9.26	9.24	9.35
XMM03297	223117	35.974476	−4.602885	0.091	zspec	41.53	−1.36	7.60	7.64	7.90
XMM03466	80641	36.062706	−5.137580	0.173	zphot	41.15	−1.04	8.03	8.27	8.04
XMM03822	218471	36.261375	−4.654545	0.854	zspec	43.24	0.78	9.29	9.24	9.68
XMM03914	383611	36.307674	−4.018576	0.149	zphot	41.47	−0.53	9.14	9.17	9.17
XMM04151	46389	36.458359	−5.237194	0.196	zphot	41.70	−0.52	8.99	9.03	9.00
XMM04366	352708	36.581959	−4.152509	0.504	zphot	42.31	0.35	9.27	9.26	9.20
XMM04379	196099	36.588135	−4.880373	0.215	zspec	41.92	−1.23	9.30	8.91	9.33
XMM04396	146862	36.595638	−4.900545	0.781	zphot	42.81	0.20	9.32	9.16	9.19
XMM04963	244870	36.905552	−4.510224	0.248	zspec	42.41	−1.44	8.77	8.69	8.81
XMM05115	33507	37.016174	−5.291483	0.321	zphot	42.14	−0.96	9.28	9.46	9.24

Note. Same as Table 2, but for XMM-LSS, and the XIDs are from Chen et al. (2018).

Figure 8 shows that our sources are generally not heavily obscured ($N_H < 10^{23}\,\mathrm{cm}^{-2}$). We plot the 95% HR upper limits for sources that are only detected in the FB (i.e., cyan downward triangles in Figure 8).[22] Although the overall constraints on their HRs are weak, most of their upper limits are still below the $N_H = 10^{23}\,\mathrm{cm}^{-2}$ region and thus disfavor high N_H. As a population, their joint HR posterior gives $\mathrm{HR} = -0.18^{+0.08}_{-0.08}$, also significantly below the $N_H = 10^{23}\,\mathrm{cm}^{-2}$ region. We note that many HR upper limits of the sources detected in the SB but not the HB in Figure 8 are above the $N_H = 10^{22}\,\mathrm{cm}^{-2}$ region but still below the $N_H = 10^{23}\,\mathrm{cm}^{-2}$

region, and the $N_H = 10^{22}\,\mathrm{cm}^{-2}$ region significantly overlaps with the $N_H = 10^{20}\,\mathrm{cm}^{-2}$ region. Therefore, we do not consider N_H thresholds lower than $10^{23}\,\mathrm{cm}^{-2}$ to mitigate the influence of these uncertainties.

This low incidence of heavy obscuration is surprising from some perspectives (e.g., Merloni et al. 2014; Liu et al. 2017). We calculate the expected number of sources with $N_H \geqslant 10^{23}\,\mathrm{cm}^{-2}$ in each field as follows:

$$\hat{n}(>10^{23}) = \sum_i \frac{\int_{23}^{24} P_{\det,i}\mathrm{XLF}_i d\log N_H}{\int_{20}^{24} P_{\det,i}\mathrm{XLF}_i d\log N_H}, \quad (13)$$

$$P_{\det,i}(N_H) = P_{\det}\left(f_X^{FB}(L_{X,i}, z_i)\beta_{FB}(N_H, z_i)\right), \quad (14)$$

$$\mathrm{XLF}_i(N_H) = \mathrm{XLF}(N_H, L_{X,i}, z_i), \quad (15)$$

where $L_{X,i}$ is the intrinsic 2–10 keV luminosity of the ith source taken from Z22, z_i is the redshift of the ith source, the intrinsic source column density N_H is in cm^{-2}, $P_{\det}$ is the detection

---

[22] Although these sources are undetected in the SB and HB, we can still provide loose constraints on their HRs. Intuitively, the fact that they are only detected in the FB but not in the SB or HB already provides some information about the underlying spectra—if their spectra were so hard that their SB counts were fully dominated by noise, it would be impossible to obtain detectable FB counts by summing fully background-dominated SB counts and undetectable (but may be excessive) HB counts; similarly, their spectra cannot be too soft. Since we are interested in how hard the spectra can be, we only show the HR upper limits for these sources.
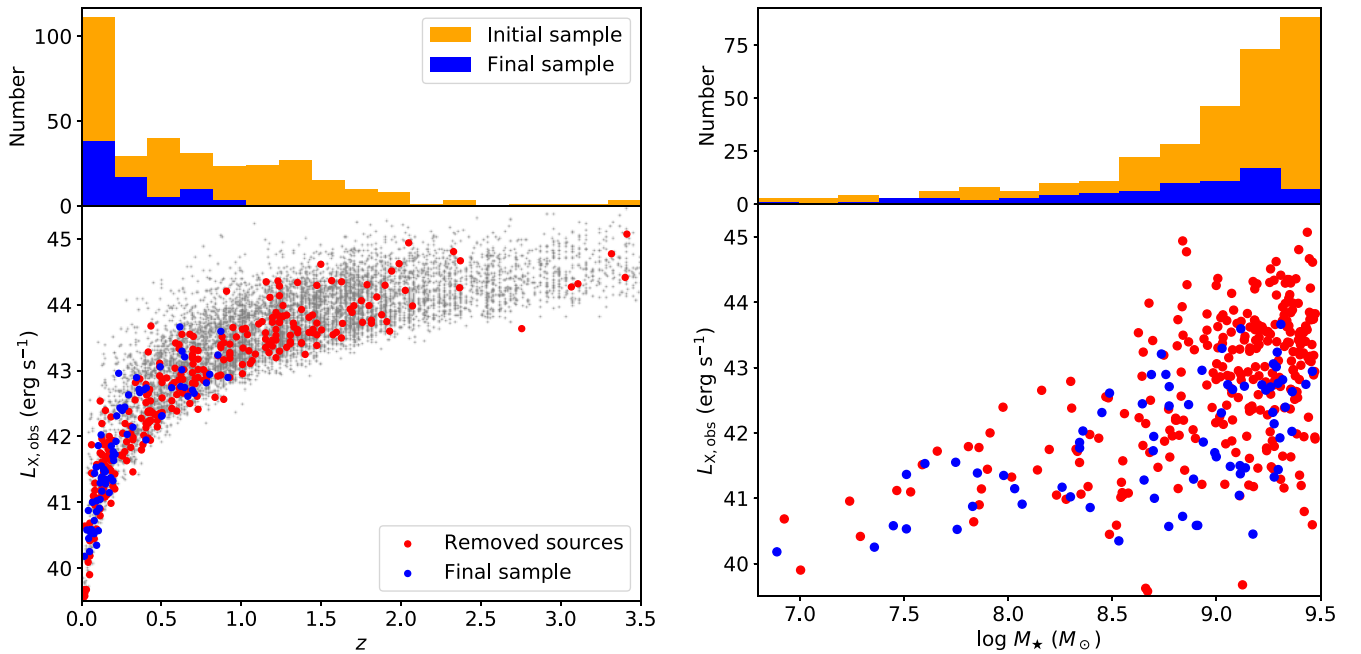
Figure 6. Left: the $z-L_{X, \text{obs}}$ plane. The gray small points are all the XMM-SERVS sources. The blue points are our final active dwarf-galaxy sample, and the red ones are those removed from the initial sample. The top histograms show the redshift distributions of the initial (orange) and final (blue) samples. Right: similar to the left panel but for the $M_\star-L_{X, \text{obs}}$ plane, and its top histograms are for the $M_\star$ distributions. Our final sample size is much smaller than the initial sample size, highlighting the overall challenges of reliably selecting distant active dwarf galaxies. Selection biases inevitably exist, especially at high redshifts.
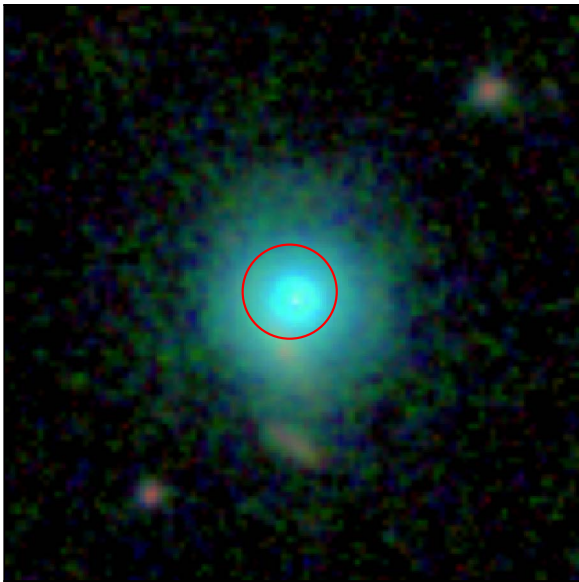
Figure 7. The three-color Hubble image of WCDFS2044 generated from F814W (blue), F125W (green), and F160W (red) images. The red circle is centered at the XMM-Newton centroid with a radius of $0\rlap{.}''5$.

probability as a function of the observed FB flux, $f_X^{\text{FB}}(L_X, z)$ is the intrinsic FB flux for a source with L_X at redshift z assuming a photon index of 1.8 and is calculated using Equation (A4) in Z22, β_{FB} is the FB absorption factor for a source with a photon index of 1.8 and is calculated based on photoelectric absorption and Compton-scattering losses (zphabs×cabs in XSPEC), XLF is the X-ray luminosity function with the N_{H} distribution included, and the summation runs over all the active dwarf galaxies. We leave the detailed derivation and explanation of P_{det} to Section 3.4. We adopt the XLF of

Ueda et al. (2014), and Z22 showed that XLFs from different works generally lead to consistent results given the XMM-SERVS depth. As in Z22, we limit the integration range of N_{H} to be below $10^{24}\,\text{cm}^{-2}$ because more heavily obscured active dwarf galaxies are generally undetectable. The above equations return $\hat{n}(>10^{23}) = 3.6$, 1.0, and 8.1 for W-CDF-S, ELAIS-S1, and XMM-LSS, respectively, which are significantly larger than our observed results in Figure 8. We find that the same conclusion still holds for our initial sample in Table 1, and thus the lack of heavily obscured sources is not caused by our selection biases.

Similar results are seen in COSMOS—Figure 5 of Mezcua et al. (2018) shows that, although mild absorption may sometimes exist, almost no sources below $z \approx 1$ (above which sources may be unreliable, as we discussed in Section 2) have sufficiently large HRs to indicate the existence of heavy obscuration. Indeed, heavily obscured active dwarf galaxies have almost not been reported even in the local universe, and Ansh et al. (2023) report the first discovery of a type 2 dwarf galaxy showing heavy X-ray obscuration. Overall, this section indicates that the massive-AGN N_{H} distribution, and consequently, the XLF, does not appear to extend down to active dwarf galaxies. This may be explained as follows. The XLF encodes the obscuration through the inverse correlation between L_X and the obscuration fraction (e.g., Brandt & Yang 2022 and references therein). However, Ricci et al. (2017) argued that the N_{H} correlation with the mass-normalized accretion rate (i.e., Eddington ratio λ_{Edd}; see Section 3.5 for more details) is more fundamental than the correlation with L_X. At a given L_X, our sources have higher λ_{Edd} than for more massive SMBHs and thus should be less obscured. Unfortunately, we cannot reliably measure λ_{Edd} due to various challenges (see Section 3.5), and thus we cannot quantitatively revise the XLF predictions of the obscuration.
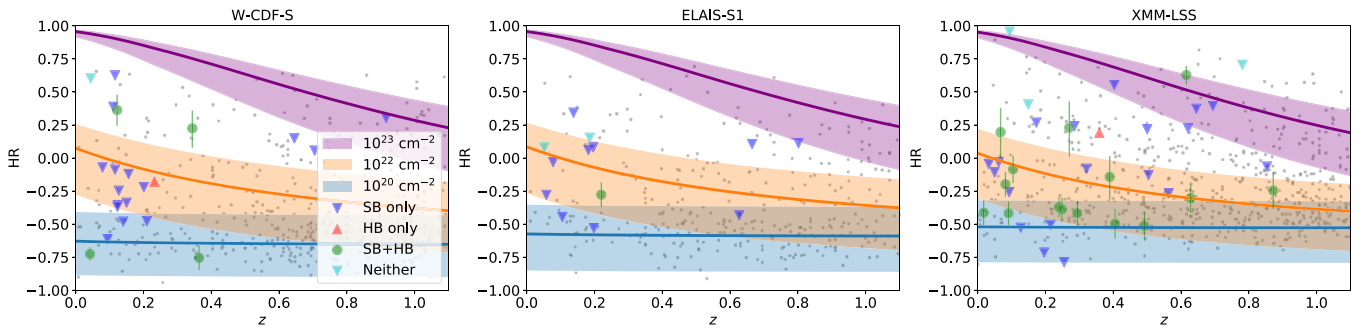
Figure 8. HR vs. z in W-CDF-S (left), ELAIS-S1 (middle), and XMM-LSS (right). The background gray points are general XMM-SERVS sources detected in both the SB and HB. The large colored points are our active dwarf galaxies, and their legend in the left panel indicates their detection status in the SB and HB. The blue downward triangles, which are detected in the SB but not the HB, represent 95% HR upper limits; while the red upward triangles, which are detected in the HB but not the SB, are 95% HR lower limits. Green points with error bars represent the median HR values with 1σ uncertainties for sources detected in both bands. The cyan downward triangles are the 95% HR upper limits for sources only detected in the FB. The shaded regions are the expected relations for redshifted absorbed power-laws, whose photon indices vary between 1.4 and 2.6, with several different $N_{\rm H}$ values, as labeled in the legend. Their corresponding solid curves mark the case when the photon index is 1.8. Our sample is generally below the $N_{\rm H} = 10^{23}$ cm^{-2} region and thus not heavily obscured in X-rays.

The right panel of Figure 8 also shows that there is one source (XID = XMM02399) above $N_{\rm H} = 10^{23}$ cm^{-2} in our XMM-LSS sample at $z = 0.6$. We will discuss this source in greater detail in Appendix B.

3.2. Radio Properties

Our fields also have deep radio coverage at 1.4 GHz from the Australia Telescope Large Area Survey (ATLAS; Franzen et al. 2015), the MeerKAT International GHz Tiered Extragalactic Exploration survey (MIGHTEE; Heywood et al. 2022), and the Very Large Array (VLA) survey in the XMM-LSS field (Heywood et al. 2020). ATLAS covers W-CDF-S and ELAIS-S1, and MIGHTEE and VLA cover XMM-LSS. These radio data have been compiled and analyzed in Zhu et al. (2023), wherein the radio sources have been matched to those in Z22.

To identify the origin of the radio emission of our sources, we define $q_{24{\rm obs}}$ as $\log(S_{24\,\mu{\rm m}}/S_{1.4\,{\rm GHz}})$, where $S_{24\,\mu{\rm m}}$ and $S_{1.4\,{\rm GHz}}$ are the observed Spitzer 24 μm and 1.4 GHz flux densities, respectively. We use $q_{24{\rm obs}}$ to identify radio-excess AGNs in our sample as outliers from the tight correlation between the FIR and radio emission. Such an FIR-radio correlation has been well constrained for star-forming galaxies over several decades (e.g., Condon 1992), and the physical reason behind it is that both the FIR and radio emission can trace SF. That is, highly star-forming galaxies simultaneously produce strong FIR and radio emission, leading to a roughly constant $q_{24{\rm obs}}$. Therefore, outliers from the FIR-radio correlation with strong excess radio emission, which can be identified if their $q_{24{\rm obs}}$ values are below a given threshold, are thought to be powered by AGNs (e.g., Ibar et al. 2008). Note, however, that $q_{24{\rm obs}}$ is not a useful indicator for other more detailed radio properties, such as morphology and radio spectral slope. We do not directly use the conventional radio-loudness parameter (e.g., Kellermann et al. 1989), which is suitable for luminous AGNs, because the implicit assumption for appropriately calculating radio-loudness is that the optical emission is dominated by AGN emission, while our sources generally do not satisfy this assumption. Therefore, classifications based on the FIR-radio correlation are often necessary and also have been shown to be currently the most effective method for selecting radio AGNs in deep surveys (e.g., Zhu et al. 2023).

We show our sources in the $z-q_{24{\rm obs}}$ plane in Figure 9, where lower or upper limits of $q_{24{\rm obs}}$ are presented for sources only detected in one band. Figure 9 also presents the $q_{24{\rm obs}}$
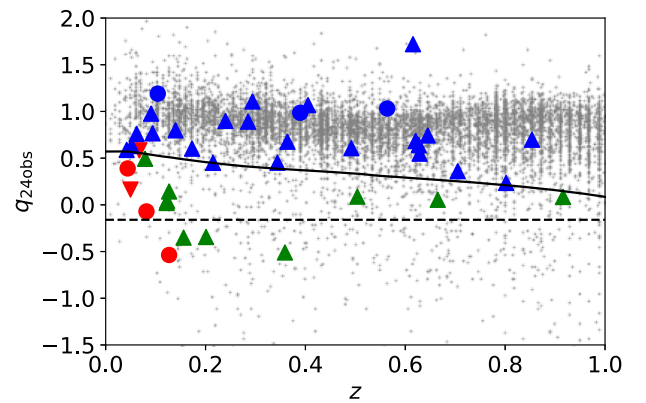

Figure 9. $q_{24{\rm obs}}$ vs. z. The black solid and dashed lines are the $q_{24{\rm obs}}$ thresholds for radio-excess AGNs in Bonzini et al. (2013) and Zhu et al. (2023), respectively. The colored points or triangles mark our active dwarf galaxies that have radio coverage and are detected in at least one of the 24 μm and 1.4 GHz bands. The points are those detected in both bands and thus have $q_{24{\rm obs}}$ values, the downward triangles represent $q_{24{\rm obs}}$ upper limits for sources only detected in the radio, and the upward triangles are $q_{24{\rm obs}}$ lower limits for sources only detected at 24 μm. Sources are colored in red if they are classified as radio-excess AGNs according to the criterion in Bonzini et al. (2013), blue if they are above the black solid line (i.e., not radio-excess AGNs), and green if unable to be classified. The background gray points are general radio sources in our fields (Zhu et al. 2023). Their photo-zs are mildly *quantized* because these photo-zs (same as those in Z22) are derived at a series of redshift grid points. This grid has a bin size of $\delta z/(1 + z) < 0.01$ and is thus sufficiently dense to avoid noticeable biases. Only a limited fraction of our sources are radio-excess AGNs.

threshold in Bonzini et al. (2013) as the black solid curve, which is 0.7 dex below the expected relation based on the redshifted M82 SED. We follow Bonzini et al. (2013) to classify a source as radio-excess if its $q_{24{\rm obs}}$ is below the curve, or its $q_{24{\rm obs}}$ upper limit (if undetected at 24 μm) is no more than 0.35 dex higher than the curve. Similarly, we classify sources as not radio excess if their $q_{24{\rm obs}}$ values or $q_{24{\rm obs}}$ lower limits (if undetected in the radio) are above the black solid curve. The remaining sources are unclassified. Five (XIDs = WCDFS0761, XMM00309, XMM00310, XMM00795, and XMM03004) of our active dwarf galaxies are radio excess, and 28 are not radio excess. However, the exact number of radio-excess sources depends on the adopted $q_{24{\rm obs}}$ threshold. If we adopt the threshold (-0.16; the black-dashed line in Figure 9) in Zhu et al. (2023), we would only have one radio-excess source (XID = XMM00309). This small incidence of radio-

excess AGNs is generally consistent with those in Mezcua et al. (2018), where 3/40 active dwarf galaxies are radio excess.

Simultaneously knowing the radio and X-ray luminosities can sometimes help measure M_{BH} through the so-called fundamental plane of BH activity, at least for some sources (e.g., Gültekin et al. 2019). However, Gültekin et al. (2022) showed that, for active dwarf galaxies, the M_{BH} inferred based on the fundamental plane is overestimated by several orders of magnitude. Our radio-excess sources have radio and X-ray luminosities similar to those in the sample in Gültekin et al. (2022) and are thus also not expected to follow the fundamental plane. Several causes that may lead to the discrepancy are discussed in detail in Gültekin et al. (2022). Especially, the fundamental plane is suggested to hold only for low-λ_{Edd} sources, but our sources may have much higher λ_{Edd} (e.g., Section 3.5). In this case, our sources are more likely to follow a different relationship, i.e., being regulated by the corona-disk-jet connection in, e.g., Zhu et al. (2020). Therefore, the radio data cannot help constrain our sources' M_{BH}.

3.3. Host Environments

It is still unclear whether and how AGN activity can affect dwarf galaxies and their environments. Unfortunately, due to the strong selection effects, especially for sSFR (Section 2.1.1), we are unable to unbiasedly assess the star formation activities of the active dwarf-galaxy population. Nevertheless, the selection effects are not directly relevant to the galaxy environment, and thus we examine if our sources and normal dwarf galaxies reside in similar environments in this section.

First, for each active dwarf galaxy with $(\log M_{\star,i}, z_i)$, we locally construct a comparison galaxy sample from Z22 by selecting galaxies with z within $(1 \pm 0.075) \times z_i$ and $\log M_\star$ within $(1 \pm 0.1) \times \log M_{\star,i}$. We do not further apply any photo-z quality cuts for these normal dwarf galaxies because their catastrophic outlier fraction is acceptably small (17.1%), although much larger than that for massive galaxies (3.9% for those with $M_\star > 10^{10.5} M_\odot$). There are typically 400 galaxies per dwarf satisfying the criterion, and we randomly pick out 100 comparison sources for each of our active dwarf galaxies. Following a similar method to Davis et al. (2022), we use projected distances to massive galaxies as an indication of the environment. We follow Yang et al. (2018a) to define the redshift slices for projections. We first calculate the dispersion of $(z_{phot} - z_{spec})/(1 + z_{spec})$, denoted as $\sigma_{\Delta z/(1+z)}$, as a function of z, from the photo-z catalogs in Chen et al. (2018) and Zou et al. (2021b). $\sigma_{\Delta z/(1+z)}$ is calculated within $z \pm 0.2$ and is roughly 0.04 for the redshift range of our sources. For each given dwarf galaxy with redshift z, we select massive galaxies with $M_\star > 10^{10.5} M_\odot$ and redshifts within $z \pm 1.5(1 + z)\sigma_{\Delta z/(1+z)}$ and calculate the first, second, third, fifth, and tenth closest projected separations between the dwarf galaxy and the massive galaxies. These separations trace the environments on 100 kpc to 1 Mpc scales. We show the corresponding histograms of the first, third, and tenth closest projected separations in Figure 10 as examples, and the histograms of our active dwarf galaxies do not visually show large differences from those of the comparison sample. Indeed, we found that our sources and the comparison samples do not show statistically significant differences for any of the separations, as also found in Davis et al. (2022) and Siudek et al. (2023). Therefore, environmental effects are not significantly responsible for the presence of AGNs in dwarf galaxies. Similar conclusions are also drawn for massive galaxies in, e.g., Yang et al. (2018a), where SMBH growth is found not to be correlated with the cosmic environment once $M_\star$ is controlled.

We also tried adding sources without X-ray excess in Section 2.2 because the exclusion of these sources may cause biases, e.g., those close to massive galaxies are more likely to be excluded. We repeated our analyses, and all the conclusions remain unchanged.

3.4. AGN Accretion Distribution and Active Fraction

In this section, we explore the distribution of AGN accretion for dwarf galaxies, which can further return the active fraction (ξ_{AGN}).[23] This is important for at least two reasons. First, the accretion distribution provides clues for how MBHs coevolve with their dwarf hosts as a population. Second, although it is generally a consensus that most massive galaxies contain SMBHs, the BH occupation fraction of dwarf galaxies is largely unknown. The active fraction serves as a lower limit for the BH occupation fraction because active sources must contain BHs. Also, due to the strong selection effects, it is difficult to select sufficient sources in $z - M_\star - L_X$ bins that are complete to calculate active fractions, and thus it is much more efficient to derive the active fraction from the accretion distribution, which is constrained by all the sources after accounting for the selection effects.

We quantify the accretion distribution as $p(L_X|M_\star, z)$, the conditional probability density per unit $\log L_X$ of a galaxy with $(M_\star, z)$ hosting an AGN with intrinsic 2–10 keV luminosity of L_X (e.g., Aird et al. 2012; Yang et al. 2018b; Aird et al. 2018). We assume a power-law relation for $p(L_X|M_\star, z)$:

$$p(L_X|M_\star, z) = A \left(\frac{M_\star}{M_0} \right)^{\gamma_M} \left(\frac{1+z}{1+z_0} \right)^{\gamma_z} \left(\frac{L_X}{L_0} \right)^{\gamma_L}, \quad (16)$$

where the normalization, A, and the power-law indices, γ_M, γ_z, and γ_L, are free parameters to be determined, and M_0, z_0, and L_0 are arbitrary scaling factors. This power-law form has been proven to be valid for massive galaxies (e.g., Aird et al. 2012), and deviations from the power law are minor and can only be revealed with sufficiently good data (Aird et al. 2018). Birchall et al. (2020, 2022) also showed that such a power law is valid for dwarf galaxies. For easy comparison with Aird et al. (2012), we adopt the same scaling factors as theirs: $M_0 = 10^{11} M_\odot$, $z_0 = 0.6$, and $L_0 = 10^{43}$ erg s^{-1}. In the following text, we consider selection effects and fit the data to constrain $p(L_X|M_\star, z)$.

We first construct a complete dwarf-galaxy sample by applying redshift-dependent $M_\star$ cuts. This is necessary because active dwarf galaxies may be subject to different incompleteness effects from inactive ones, and it is difficult to correct the incompleteness of the active population independently from the normal population. To estimate the $M_\star$ depth, we first adopt the limiting VIDEO K_s-band magnitude as $K_{s,lim} = 23.1$ mag, the $5\sigma K_s$ depth in a $3''$ aperture. This limit is conservative for two reasons. First, the nominal magnitude depth becomes deeper with decreasing aperture size, and a $3''$ aperture may be large. As a comparison, the K_s-band depth of a $1''$ aperture is 1.5 mag deeper. Second, other VIDEO bands may reach deeper depths

---

[23] The term *active fraction* should be distinguished from the term *fractional AGN contribution* used in Section 2.1. We used "f_{AGN}" to denote the latter and will use "ξ_{AGN}" to denote the former in this section.
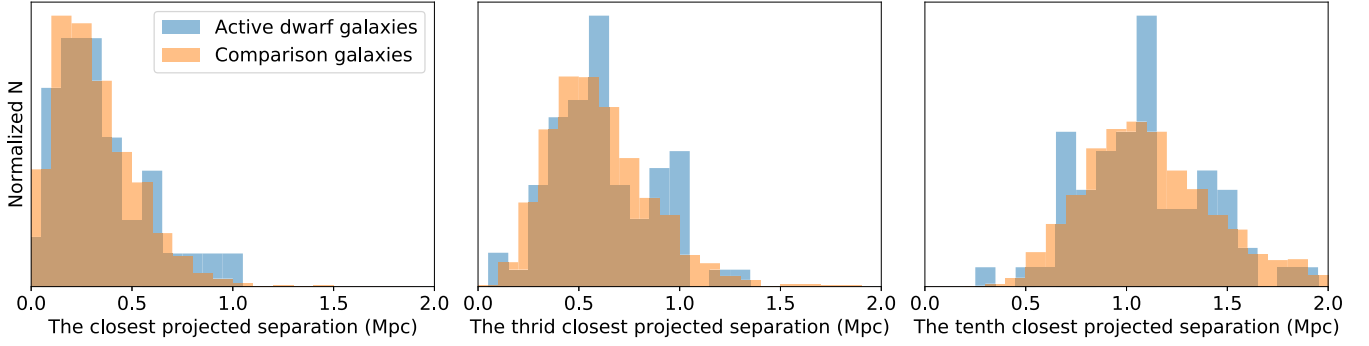
Figure 10. The normalized histograms of the first (left), third (middle), and tenth (right) closest projected separations of dwarf galaxies with respect to massive galaxies. Our active dwarf galaxies do not show clear differences from their comparison samples.

than K_s. Due to these reasons, less than half of the sources in Z22 are more massive than the limiting $M_\star$ derived below. Nevertheless, this ensures that the samples are complete. Following Pozzetti et al. (2010), we then convert the magnitude depth to the expected limiting $M_\star$ for each K_s-detected galaxy in Z22: $\log M_{\rm lim} = \log M_\star + 0.4(K_s - K_{s,\rm lim})$. At each redshift, we adopt the $M_\star$ completeness threshold as the value above which 90% of the $M_{\rm lim}$ values lie. We derive the limiting $M_\star$ for all three XMM-SERVS fields independently, and Figure 11 presents the corresponding curves as functions of z. The curves in different fields are generally consistent. 54 out of the 73 active dwarf galaxies are above the completeness curves, and all the sources beyond $z \approx 0.8$ are subject to incompleteness. As in Section 3.3, we do not apply photo-z quality cuts for normal dwarf galaxies. The catastrophic outlier fraction is much smaller than the uncertainties of our parameters, as will be measured in the following text (Table 5).

After settling the selection effects upon $M_\star$, we further quantify those from the XMM-SERVS survey, i.e., the probability that a source with observed FB flux of $f_{\rm X,obs}^{\rm FB}$ gets detected by the survey, which is denoted as $P_{\rm det}(f_{\rm X,obs}^{\rm FB})$. A common way of deriving $P_{\rm det}$ is to use the sensitivity curves and estimate $P_{\rm det}(f_{\rm X,obs}^{\rm FB})$ as the fraction of the total survey area with sensitivities deeper than $f_{\rm X,obs}^{\rm FB}$. However, this approach can cause biases because the sensitivity is derived for a given aperture ($20'' \times 20''$ for XMM-SERVS) while the real detection procedures are more complicated and cannot be accurately mimicked by a Poisson detection in a given constant aperture. We thus derive $P_{\rm det}$ by comparing the intrinsic $\log N - \log S$ relation in Georgakakis et al. (2008) and the cataloged flux distribution, where the $\log N - \log S$ relation is the well-determined expected observed flux distribution with the detection procedures deconvolved, given by $dN/df_{\rm X}^{\rm FB}$, the surface number density per unit $f_{\rm X}^{\rm FB}$. We assume a functional formula[24] for $P_{\rm det}$:

$$P_{\rm det}(f_{\rm X,obs}^{\rm FB}) = \frac{1}{2}[{\rm erf}(b(\log f_{\rm X,obs}^{\rm FB} - a)) + 1], \qquad (17)$$

where a and b are free parameters to constrain, and the same functional formula has been adopted for optical surveys (e.g., Bernstein et al. 2004). The log-likelihood (e.g., Barlow 1990;

----

[24] We found it necessary to adopt a functional formula instead of estimating $P_{\rm det}$ in some $\log f_{\rm X,obs}$ bins because the limited number of high-$f_{\rm X,obs}$ sources cannot provide effective constraints to $P_{\rm det}$ when $f_{\rm X,obs}$ is high. We have also confirmed that this formula works well and is in perfect consistency with the binned estimations of $P_{\rm det}$ in $\log f_{\rm X,obs}$ bins with sufficient sources.

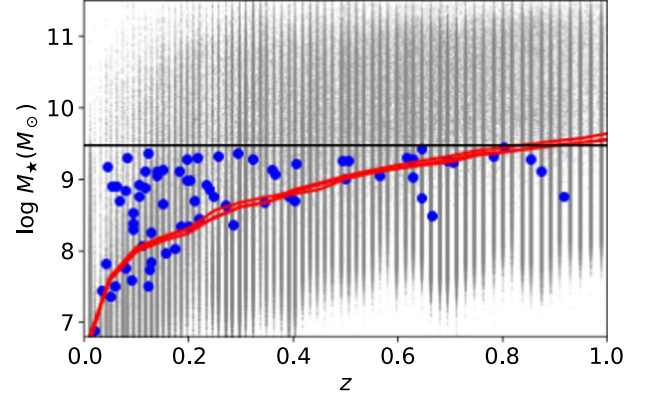**Figure 11.** $M_\star$ vs. z. The background gray points are all the sources in Z22, the blue points are our final active dwarf-galaxy sample, and the three red curves, which visually overlap with each other, are the $M_\star$ completeness curves for our three fields. Sources above the red curves are utilized to constrain the accretion distribution and active fraction of the dwarf-galaxy population.

Table 5
Fitting Results of the Accretion Distribution Model

		$\log A$	γ_M	γ_z	γ_L
Case P	Merged	$-3.02_{-0.24}^{+0.25}$	$0.56_{-0.13}^{+0.13}$	$2.35_{-1.74}^{+1.75}$	$-0.91_{-0.11}^{+0.11}$
	W-CDF-S	$-3.50_{-0.56}^{+0.54}$	$0.73_{-0.22}^{+0.23}$	$-3.34_{-4.39}^{+4.33}$	$-0.90_{-0.23}^{+0.20}$
	ELAIS-S1	$-3.27_{-0.50}^{+0.48}$	$0.46_{-0.27}^{+0.27}$	$7.06_{-3.94}^{+3.90}$	$-1.14_{-0.28}^{+0.26}$
	XMM-LSS	$-2.89_{-0.35}^{+0.37}$	$0.49_{-0.19}^{+0.20}$	$2.30_{-2.18}^{+2.28}$	$-0.79_{-0.14}^{+0.13}$
Case C	Merged	$-2.10_{-0.15}^{+0.16}$	$0.70_{-0.08}^{+0.09}$	$3.86_{-0.98}^{+0.95}$	$-0.94_{-0.07}^{+0.06}$
	W-CDF-S	$-2.16_{-0.27}^{+0.28}$	$0.70_{-0.15}^{+0.16}$	$3.68_{-1.75}^{+1.74}$	$-0.95_{-0.13}^{+0.12}$
	ELAIS-S1	$-1.73_{-0.25}^{+0.26}$	$0.91_{-0.14}^{+0.15}$	$2.92_{-1.71}^{+1.69}$	$-0.97_{-0.11}^{+0.11}$
	XMM-LSS	$-2.41_{-0.26}^{+0.27}$	$0.50_{-0.15}^{+0.15}$	$5.28_{-1.61}^{+1.67}$	$-0.95_{-0.11}^{+0.11}$

Loredo 2004) when compared with the survey catalogs is

$$\ln \mathcal{L} = -A_{\rm tot} \int \frac{dN}{df_{\rm X,obs}^{\rm FB}} P_{\rm det} df_{\rm X,obs}^{\rm FB} + \sum_i \ln P_{\rm det}(f_{i,\rm obs}^{\rm FB}), \quad (18)$$

where constants independent from $P_{\rm det}$ are discarded, $A_{\rm tot}$ is the survey area, $f_{i,\rm obs}^{\rm FB}$ is the observed FB flux of the ith FB-detected source in the XMM-SERVS catalogs, and the summation runs over all the FB-detected sources. We only consider the regions overlapping with the VIDEO footprints and minimize the likelihood for each field independently to measure a and b. The results are $(a, b) = (-14.36, 4.85)$, $(-14.30, 3.80)$, and $(-14.42, 4.38)$ for W-CDF-S, ELAIS-S1, and XMM-LSS, respectively. We adopt the detection probability in the FB

because most of our active dwarf galaxies are detected in the FB. Among the 54 sources above the $M_\star$ completeness, five are not detected in the FB. It is challenging to quantify the probability of not detecting a source in the FB but detecting it in another band because more detailed spectral shapes should be considered, and thus we remove the five FB-undetected sources from our following analyses for simplicity.

Overall, we use all the 49 active dwarf galaxies above the $M_\star$ completeness threshold and detected in the FB to constrain $p(L_X|M_\star, z)$. The log-likelihood function (e.g., Aird et al. 2012; Yang et al. 2018b) is

$$\ln \mathcal{L} = -n_{\rm mdl} + \sum_{i=1}^{n_{\rm AGN}} \ln p(L_{X,i}|M_{\star,i}, z_i), \qquad (19)$$

where the summation is for our 49 active dwarf galaxies, and $n_{\rm mdl}$ is the expected number of FB-detected active dwarf galaxies given a model parameter set. The log-likelihood is calculated in all three fields separately and added together to a merged log-likelihood function. $n_{\rm mdl}$ is

$$n_{\rm mdl} = \sum_{i=1}^{n_{\rm gal}} \int_{-\infty}^{+\infty} p(L_X|M_{\star,i}, z_i) P_{\rm det}(f_X^{\rm FB}) d\log L_X, \qquad (20)$$

where $f_X^{\rm FB} = f_X^{\rm FB}(L_X, z)$ is the intrinsic FB flux for a source with L_X at redshift z assuming a photon index of 1.8, as in Section 3.1. Given our parameterization, the above equation can be solved analytically. The key is using the following integration (Ng & Geller 1969):

$$\int e^{cx}[\mathrm{erf}(x) + 1] dx = \frac{1}{c}\left\{ e^{cx}[\mathrm{erf}(x) + 1] - e^{\frac{c^2}{4}} \mathrm{erf}\left(x - \frac{c}{2}\right) \right\}. \qquad (21)$$

Then the derivations become straightforward, and Equation (20) can be reduced to the following form when $\gamma_L < 0$:

$$n_{\rm mdl} = -\frac{\exp\left(\left(\frac{\gamma_L \ln 10}{2b}\right)^2\right)}{\gamma_L \ln 10} \sum_{i=1}^{n_{\rm gal}} p(L_X(10^a, z_i)|M_{\star,i}, z_i), \qquad (22)$$

where $L_X(f_X^{\rm FB}, z)$ is the inverse function of $f_X^{\rm FB}(L_X, z)$. Using Equation (22) instead of numerically solving the integration in Equation (20) increases the computational speed by several orders of magnitude.

Unlike Aird et al. (2012), who set a lower limit of $L_X = 10^{42}$ erg s^{-1} for the integration in Equation (20), we set the lower integration limit as $-\infty$. This effectively means that we regard all the dwarf galaxies that are detectable given the XMM-SERVS sensitivity to be powered by AGNs, which is supported in Section 2.2—the expected galaxy emission from all the X-ray-detected dwarf galaxies (not accounting for the emission from nearby sources) is far smaller than the observed fluxes. Note that we neglect the intrinsic obscuration because, as shown in Section 3.1, active dwarf galaxies do not have a suitable a priori XLF available and generally are not heavily obscured. To quantitatively assess the possible impact of obscuration, we calculate the expected mean absorption factor

predicted by the XLF in Ueda et al. (2014) as follows:

$$E\{\langle \log \beta_{\rm FB} \rangle\} = \frac{1}{n_{\rm AGN}} \sum_{i=1}^{n_{\rm AGN}} \frac{\int_{20}^{24} \log \beta_{\rm FB} P_{{\rm det},i} {\rm XLF}_i d\log N_{\rm H}}{\int_{20}^{24} P_{{\rm det},i} {\rm XLF}_i d\log N_{\rm H}}, \qquad (23)$$

where $P_{{\rm det},i}(N_{\rm H})$ and ${\rm XLF}_i(N_{\rm H})$ are defined in Equations (14) and (15), respectively. This returns $E\{\langle \log \beta_{\rm FB} \rangle\} = -0.24$ dex, causing $\log A$ to shift by $|\gamma_L E\{\langle \log \beta_{\rm FB} \rangle\}| \approx 0.2$ dex, where $\gamma_L = 0.9$, as will be measured in the following text (Table 5). Such a difference is comparable to the 1σ uncertainty of $\log A$ in Table 5. The actual absorption factor should be far smaller than the XLF-predicted value (Section 3.1), and thus neglecting the intrinsic obscuration will not cause more than 1σ difference in our results.

We adopt a flat prior on $(\log A, \gamma_M, \gamma_z, \gamma_L)$ while restricting $\gamma_L < 0$ and use `DynamicHMC.jl`,[25] a package implementing Hamiltonian Monte Carlo (e.g., Betancourt 2017), to sample the posterior. We apply the analyses to our final active dwarf-galaxy sample, as presented above in the previous part of this section before this paragraph, and denote this case as Case P, where "P" stands for "purity." However, this sample is designed to be pure instead of complete, and hence we may underestimate the active fraction. We thus regard the active fractions derived from this case as lower limits. We also conduct the same analyses on the initial sample in Table 1, which should be complete but not pure, and regard the corresponding active fractions as upper limits. We denote this case as Case C, where "C" stands for "completeness," and there are 149 FB-detected active dwarf galaxies above the $M_\star$ completeness curve. In each case, we also conduct the same analyses in each field to check the consistency.

We present the sampling results in Figure 12, based on which we report the fitted parameters in Table 5. The contours for Case C look similar aside from systematic differences in some parameters and are thus not plotted in Figure 12 for clarity. The $\log A - \gamma_M$ and $\gamma_z - \gamma_L$ contours are highly tilted, indicating that their uncertainties are correlated. The same analyses are also applied to individual fields, and their results in Table 5 are statistically consistent with each other, indicating that there are no significant inter-field systematic biases that are larger than the statistical fluctuations. When comparing the merged results in Cases P and C, their γ_M, γ_z, and γ_L are in good agreement, while Case C has a larger $\log A$ value than Case P because more active dwarf galaxies are included.

To help visualize the comparison between the model and the data, we use the $n_{\rm obs}/n_{\rm mdl}$ method to obtain binned estimators of $p(L_X|M_\star, z)$, as outlined in Aird et al. (2012), which overcomes significant variations of the model within a bin and X-ray selection effects by applying model-dependent corrections. We select four bins in the $z - M_\star$ plane that are above the $M_\star$ completeness curves and below $M_\star = 3 \times 10^9 M_\odot$: z range$\times \log M_\star$ range = $[0, 0.25] \times [9, 9.5]$, $[0.25, 0.5] \times [9, 9.5]$, $[0, 0.25] \times [8.5, 9]$, and $[0, 0.12] \times [8, 8.5]$. In each bin, we denote the number of observed active dwarf galaxies as $n_{\rm obs}$ and calculate the model-predicted number as $n_{\rm mdl}$ using Equation (20). The binned estimator of $p(L_X|M_\star, z)$ is then the fitted model evaluated at a given $(M_\star, z, L_X)$ scaled by $n_{\rm obs}/n_{\rm mdl}$, and its uncertainty is calculated from the Poisson

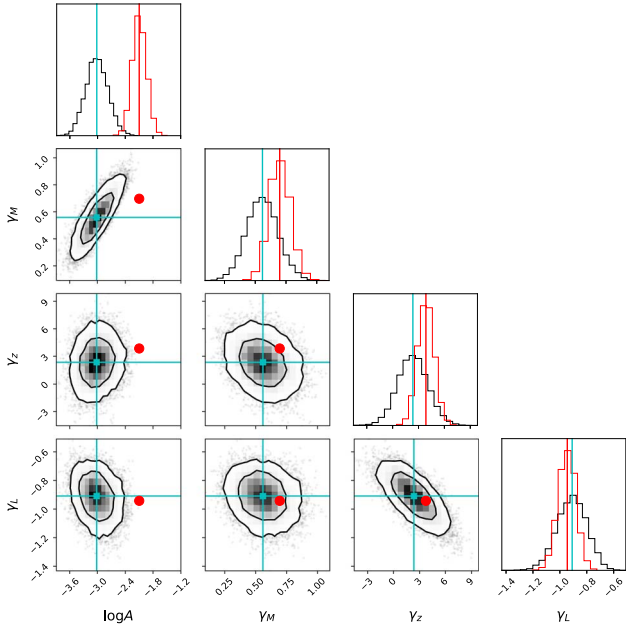---

[25] https://www.tamaspapp.eu/DynamicHMC.jl/stable/

Figure 12. The sampling results of the accretion distribution parameters. In the upper panels, the black and red histograms are for the sampling distributions in Cases P and C, respectively; the cyan and red vertical lines mark the corresponding median values. In the other panels, the sampling points and contours are for Case P, and those for Case C are not shown for better visualization. The black contours represent 68% and 95% levels in Case P, the grayscale pixels represent probabilities, and the rasterized points outside the 95% contours are individual sampling points. The median sampling values in Case P are shown as the cyan squares and lines, and those in Case C are displayed as the large red points. The results in Cases P and C mainly differ in $\log A$, and their γ_z and γ_L are consistent.

error of n_{obs}. We present our fitted model and the binned estimators in Figure 13, and they are consistent and both indicate that $p(L_{\mathrm{X}}|M_\star, z)$ increases with $M_\star$.

In both Cases P and C, our γ_M (γ_L) is positive (negative) above a 3σ confidence level,[26] indicating that, at fixed L_{X}, dwarf galaxies have larger probabilities of hosting AGNs with increasing $M_\star$, and the probability decreases as L_{X} increases. Although most of our fitted γ_z values are positive, the evidence is not sufficiently strong to confirm positive redshift evolution in Case P due to the large statistical uncertainties of γ_z. Aird et al. (2012) conducted the same analyses for massive galaxies, and our fitted γ_M, γ_z, and γ_L values are consistent with theirs, possibly indicating that the factors causing these dependencies in dwarf galaxies are similar to those in massive galaxies. However, our normalization, A, is significantly smaller than that in Aird et al. (2012) in Case P and only marginally consistent with Aird et al. (2012) in Case C.

We further compare our ξ_{AGN} with previous work. ξ_{AGN} is generally poorly defined and often strongly depends on the AGN selection techniques and survey depths. However, under our accretion distribution context, ξ_{AGN} has an unambiguous definition, which enables direct comparisons with previous work that also adopts the same definition. ξ_{AGN} within a given

---

L_{X} range, $(L_{\mathrm{X,low}}, L_{\mathrm{X,high}})$, is defined as follows:

$$\xi^L_{\mathrm{AGN}}(M_\star, z) = \int_{\log L_{\mathrm{X,low}}}^{\log L_{\mathrm{X,high}}} p(L_{\mathrm{X}}|M_\star, z)\, d\log L_{\mathrm{X}}, \qquad (24)$$

where $L_{\mathrm{X,high}}$ is allowed to reach infinity, and we add a superscript "L" to indicate that the definition is based on luminosity. A common alternative definition is based on the specific BH accretion rate (λ_{sBHAR}; e.g., Aird et al. 2018; Birchall et al. 2020, 2022), which is defined as follows:

$$\lambda_{\mathrm{sBHAR}} = \frac{25 L_{\mathrm{X}}}{1.26 \times 10^{38} \times 0.002 M_\star}, \qquad (25)$$

where the multiplicative constants are chosen so that $\lambda_{\mathrm{sBHAR}} \approx \lambda_{\mathrm{Edd}}$ (Section 3.5) for massive galaxies that follow the relation between M_{BH} and the galaxy bulge mass. $p(L_{\mathrm{X}}|M_\star, z)$ can then be converted to $p(\lambda_{\mathrm{sBHAR}}|M_\star, z)$:

$$p(\lambda_{\mathrm{sBHAR}}|M_\star, z) = A\left(\frac{M_\star}{M_0}\right)^{\gamma_M + \gamma_L}\left(\frac{1+z}{1+z_0}\right)^{\gamma_z}\left(\frac{\lambda_{\mathrm{sBHAR}}}{\lambda_0}\right)^{\gamma_L}, \qquad (26)$$

where $\lambda_0 = \lambda_{\mathrm{sBHAR}}(L_{\mathrm{X}} = L_0, \quad M_\star = M_0)$. Similar to Equation (24), ξ_{AGN} within a given λ_{sBHAR} range, $(\lambda_{\mathrm{sBHAR,low}}, \lambda_{\mathrm{sBHAR,high}})$, is defined as follows:

$$\xi^\lambda_{\mathrm{AGN}}(M_\star, z) = \int_{\log \lambda_{\mathrm{sBHAR,low}}}^{\log \lambda_{\mathrm{sBHAR,high}}} p(\lambda_{\mathrm{sBHAR}}|M_\star, z)\, d\log \lambda_{\mathrm{sBHAR}}, \qquad (27)$$

where we add a superscript "λ" to indicate that the definition is based on λ_{sBHAR}. We show ξ_{AGN} as a function of $M_\star$ in Figure 14, where we evaluate it at our median redshift, 0.2. We adopt two different AGN definitions, $L_{\mathrm{X}} > 10^{42}\,\mathrm{erg\,s^{-1}}$ (Aird et al. 2012) and $\lambda_{\mathrm{sBHAR}} > 0.01$ (Aird et al. 2018). The figure reveals that ξ^L_{AGN} increases with $M_\star$ and is systematically lower than the model in Aird et al. (2012; their Table 2), though the difference is small in Case C. However, $\xi^\lambda_{\mathrm{AGN}}$ is more independent of $M_\star$ and more consistent with the model in Aird et al. (2012; their Table 3). The normalizations of ξ_{AGN} in the two panels of Figure 14 also differ by $\gtrsim 1$ dex—ξ^L_{AGN} is roughly between 10^{-5} and 10^{-3}, while $\xi^\lambda_{\mathrm{AGN}}$ is roughly between 10^{-3} and 10^{-2}. These are consistent with the local universe results in Birchall et al. (2022); the strong positive correlation between ξ^L_{AGN} and $M_\star$ is at least partly driven by the positive correlation between M_{BH} and $M_\star$, and the specific accretion rate does not necessarily strongly correlate with $M_\star$. Nevertheless, it is unclear if adopting $\xi^\lambda_{\mathrm{AGN}}$ can fully eliminate this factor, and Section 3.5 will discuss related problems that may cause λ_{sBHAR} to systematically deviate from λ_{Edd} for dwarf galaxies.

We further present more comprehensive comparisons in Figure 15. First, we estimate ξ_{AGN} in a given mass-complete $z-M_\star$ bin as follows:

$$\xi_{\mathrm{AGN}} = \frac{1}{n_{\mathrm{gal}}} \sum_{i=1}^{n_{\mathrm{gal}}} \xi_{\mathrm{AGN}}(M_i, z_i), \qquad (28)$$

where the summation runs over all the sources in the bin. For easier comparisons with Mezcua et al. (2018), we estimate ξ_{AGN} in the same two L_{X} bins adopted in Mezcua et al. (2018):
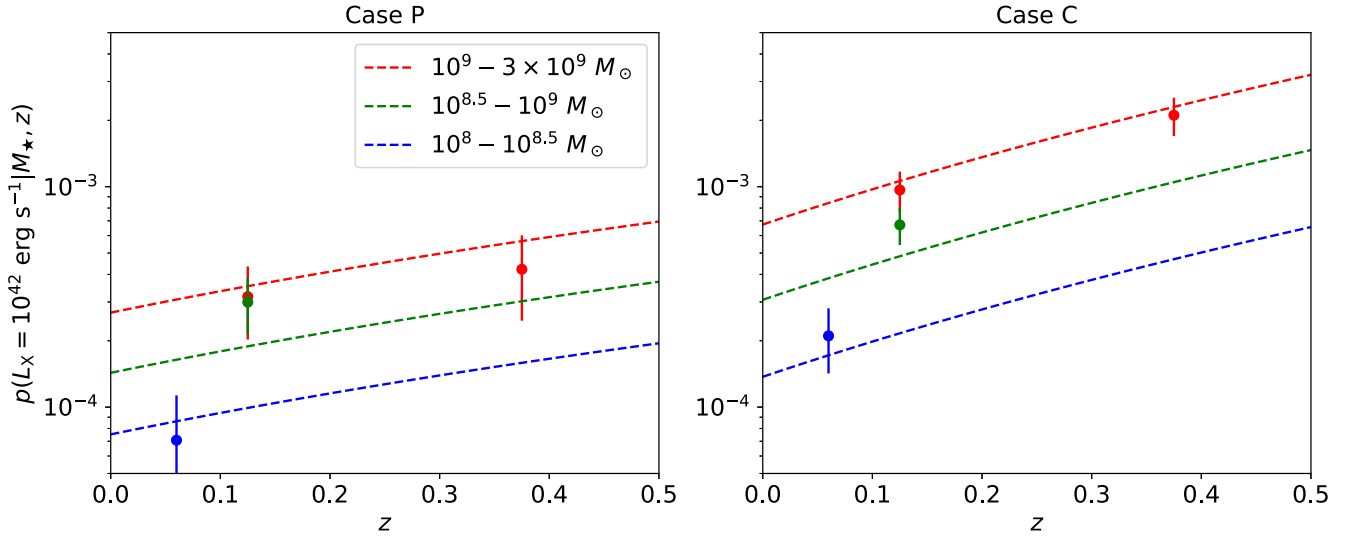
Figure 13. Our fitted $p(L_X|M_\star, z)$ model (dashed lines) and the corresponding four binned estimators based on our data (points with error bars) as functions of z. The model and binned estimators are both evaluated at $L_X = 10^{42}$ erg s^{-1} and the $M_\star$ bin centers. The left and right panels are for Cases P and C, respectively. Our model is consistent with the binned estimators.
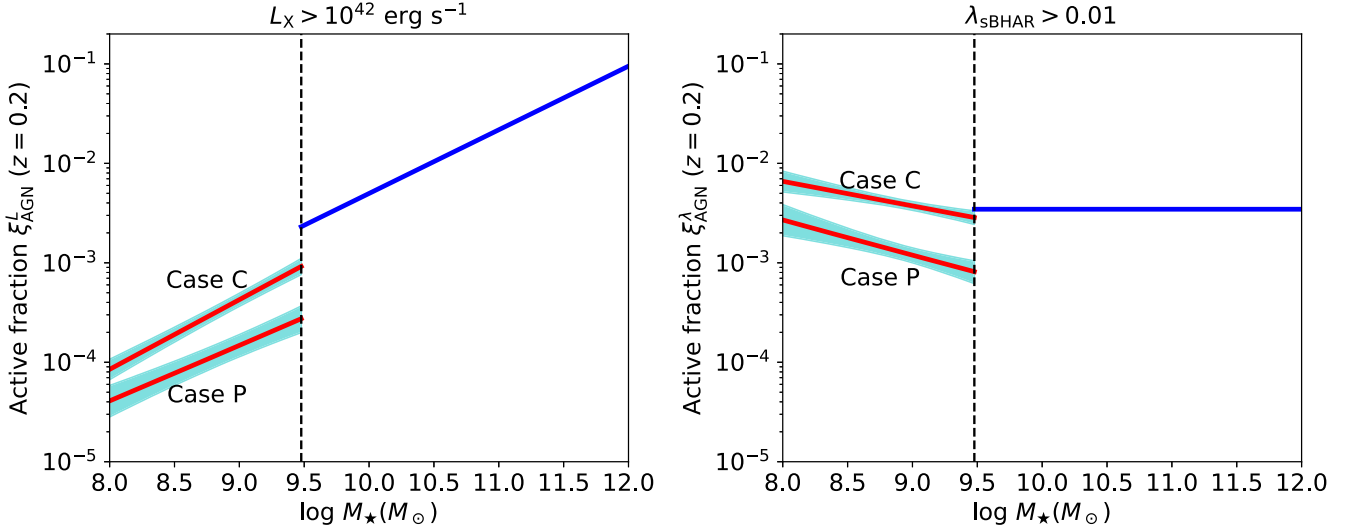

Figure 14. $\xi_{\rm AGN}$ as a function of $M_\star$, where the AGN definitions are presented as the panel titles, and the models are evaluated at our median redshift (0.2). The vertical dashed lines mark the $M_\star$ definitions ($3 \times 10^9 M_\odot$) of dwarf galaxies. The models in this work are presented as red lines with cyan regions showing 1σ confidence ranges, and blue lines are for massive galaxies, taken from Aird et al. (2012).

$3.7 \times 10^{41} \leqslant L_{0.5-10\,{\rm keV}} < 2.4 \times 10^{42}$ erg s^{-1} and $L_{0.5-10\,{\rm keV}} \geqslant 2.4 \times 10^{42}$ erg s^{-1}, where $L_{0.5-10\,{\rm keV}}$ is converted from L_X assuming a photon index of 1.8. We present our $\xi_{\rm AGN}$ estimations in Figure 15, where we also display previous estimations from Reines et al. (2013), Schramm et al. (2013), Pardo et al. (2016), Aird et al. (2018), and Mezcua et al. (2018). There are several more works presenting $\xi_{\rm AGN}$ (e.g., Baldassare et al. 2020b; Birchall et al. 2020; Latimer et al. 2021; Birchall et al. 2022; Ward et al. 2022), and they are mainly limited to the local universe. We do not show them in Figure 15 to avoid crowding, and interested readers can refer to these articles for more details. Note that due to different and sometimes unknown underlying definitions in most articles from ours, quantitative comparisons are meaningful only with the results in Mezcua et al. (2018). The figure shows that our binned $\xi_{\rm AGN}$ values are generally consistent with those in previous literature.

Our constraints should be the best given our larger sample size and the fact that we have thoroughly identified multiple underlying issues in Section 2. Both Table 5 and Figure 15 do not indicate statistically significant redshift evolution of $\xi_{\rm AGN}$ for dwarf galaxies. Similar conclusions have been drawn in previous works (Aird et al. 2018; Mezcua et al. 2018; Birchall et al. 2022). However, the large statistical uncertainties may have hindered us from detecting any possible trend, and a larger sample with at least a few hundred objects is needed to provide more meaningful constraints.

3.5. Bolometric Luminosity, BH Mass, Eddington Ratio, and the Underlying Challenges

We try to assess the AGN bolometric luminosities ($L_{\rm bol}^{\rm AGN}$), $M_{\rm BH}$, and $\lambda_{\rm Edd}$ of our sources in this section. $\lambda_{\rm Edd}$ quantifies the

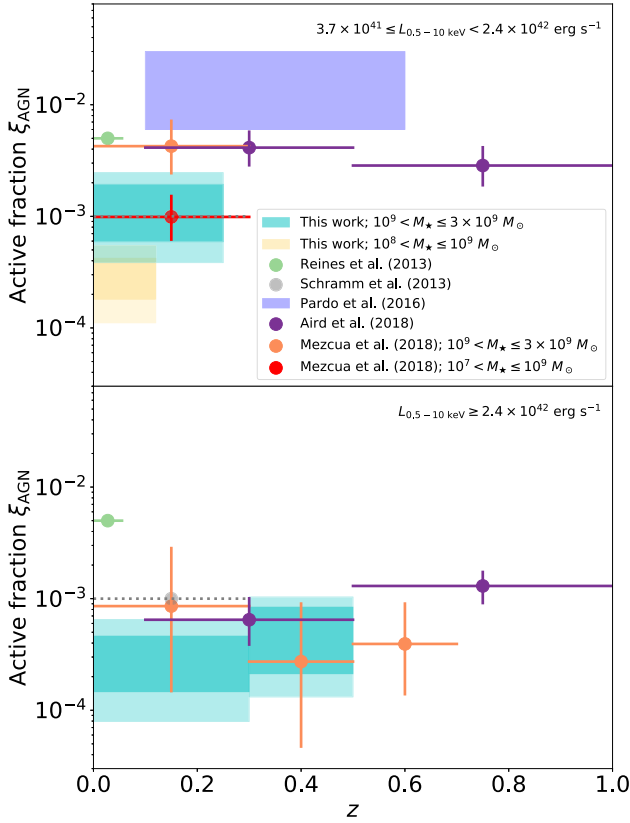**Figure 15.** ξ_{AGN} in several $z-M_\star-L_X$ bins compared with previous works, adapted from Figure 10 in Mezcua et al. (2018). The top and right panels are for $3.7 \times 10^{41} \leqslant L_{0.5-10\,keV} < 2.4 \times 10^{42}$ erg s^{-1} and $L_{0.5-10\,keV} \geqslant 2.4 \times 10^{42}$ erg s^{-1}, respectively. Our measurements are shown as the cyan $(10^9 < M_\star \leqslant 3 \times 10^9\,M_\odot)$ and yellow $(10^8 < M_\star \leqslant 10^9\,M_\odot)$ boxes, whose redshift ranges are chosen so that the corresponding boxes are above the $M_\star$ completeness curves and if possible, match those in Mezcua et al. (2018) for easy comparison. The parts with darker colors within the cyan and yellow boxes represent the ξ_{AGN} values calculated from the fitted model parameters in Case P (lower boundaries) and Case C (upper boundaries), and the outskirts with lighter colors are delimited by the lower 2σ sampling values of ξ_{AGN} in Case P (lower boundaries) and upper 2σ values of ξ_{AGN} in Case C (upper boundaries). Our ξ_{AGN} is generally consistent with those in previous works.

relative accretion power and is defined as follows:

$$\lambda_{Edd} = \frac{L_{bol}^{AGN}}{L_{Edd}} = \frac{L_{bol}^{AGN}/(\text{erg s}^{-1})}{1.26 \times 10^{38} M_{BH}/M_\odot}. \quad (29)$$

We adopt L_{bol}^{AGN} as the likelihood-weighted angle-averaged intrinsic AGN disk luminosity based on the SED fitting in Z22. We do not add the corona luminosity in X-rays into L_{bol}^{AGN} because we usually expect that the disk luminosity dominates, and more importantly, as we will see later, only adopting the disk luminosity can help appreciate some important features. We then estimate M_{BH} based on the $M_{BH}-M_\star$ scaling relation in Reines & Volonteri (2015): $\log(M_{BH}/M_\odot) = 7.45 + 1.05[\log(M_\star/M_\odot) - 11]$. The scatter of the relation is significant (0.55 dex). We plot M_{BH} versus L_{bol}^{AGN} in Figure 16, in which several constant-λ_{Edd} lines are shown for comparison. We also plot a typical L_{bol}^{AGN} limit corresponding to a typical FB X-ray detection limit of $10^{-14.4}$ erg cm^{-2} s^{-1} (see Section 3.4), a redshift of our median value (0.2), and a typical AGN bolometric correction ($k_{bol}^{AGN} = L_{bol}^{AGN}/L_X$) of 16.75, the low-mass limit of k_{bol}^{AGN} in Duras et al. (2020). The figure indicates that the inferred M_{BH} values range between $\approx 10^4$ and $10^6\,M_\odot$ with a median value of $2 \times 10^5\,M_\odot$ and thus at least some

fraction are in the IMBH regime. Our sources, with a median λ_{Edd} value of 0.19, are often close to or are Eddington-limited. These high λ_{Edd} values are consistent with the findings in Mezcua et al. (2018), as largely expected because the involved X-ray surveys have similar depths and will preferentially select high-λ_{Edd} sources.

To further check the reliability, we show our sources in the $\lambda_{Edd} - k_{bol}^{AGN}$ plane in Figure 17. For SMBHs, k_{bol}^{AGN} depends on λ_{Edd} because the corona emission becomes relatively weaker as λ_{Edd} increases. Lusso et al. (2012) and Duras et al. (2020) presented the calibrated correlation between the two quantities for massive SMBHs ($M_{BH} \approx 10^7-10^9\,M_\odot$) with strong accretion ($\lambda_{Edd} \approx 0.01-1$), and these relations are also presented in Figure 17. Our sample significantly deviates from the expected relations, indicating that the overall estimations of the relevant parameters are problematic. We call this inconsistency the "λ_{Edd} tension" hereafter. Since L_X is largely robust, one or more of the following three factors must be wrong: L_{bol}^{AGN} estimations, M_{BH} estimations, and the $\lambda_{Edd} - k_{bol}^{AGN}$ relation. We will discuss these in the following text. As we will see, all three factors may have severe issues, and thus the ultimate goal of this section is not to accurately measure λ_{Edd} for our sample, but to point out the problems that should be solved before the measurement and subsequent scientific discussions.

3.5.1. Challenges That May Lead to the λ_{Edd} Tension

L_{bol}^{AGN} is involved in both λ_{Edd} and k_{bol}^{AGN}, and changing L_{bol}^{AGN} will cause the points in Figure 17 to move along lines with slopes of unity in the $\log \lambda_{Edd} - \log k_{bol}^{AGN}$ plane. The red star with an intersecting red line in Figure 17 shows the median among our sources with $\lambda_{Edd} \geqslant 0.1$ and the corresponding trajectory when systematically varying L_{bol}^{AGN}. The lower left part of Figure 17 is occupied by sources with $\lambda_{Edd} \lesssim 0.1$ and unphysically small k_{bol}^{AGN} that roughly form a trend parallel to the red line, indicating that these sources may have underestimated L_{bol}^{AGN} values. Figure 17 indicates that the λ_{Edd} tension would be mitigated by systematically increasing L_{bol}^{AGN}. The first challenge of the L_{bol}^{AGN} estimations is that, as pointed out in Section 3.2.4 of Z22, it is difficult to reliably constrain the strength of the AGN component unless the AGN emission dominates. Z22 argued that this is a fundamental problem in SED fitting limited by the data and can hardly be solved merely with more sophisticated methods. The other problem arises from the fundamental fact that the accretion disk temperature becomes higher as M_{BH} decreases ($\propto M_{BH}^{-\frac{1}{4}}$). This causes a large amount of the disk emission to occur at extreme-UV (EUV) energies that are neither covered by our SED photometry nor the assumed disk SED model[27] (e.g., Cann et al. 2018).

We use the Shakura–Sunyaev (SS) standard thin accretion disk (Shakura & Sunyaev 1973) to illustrate the second problem. Even if the SS disk is not exactly applicable, it illustrates the relevant trends; but also note that the standard accretion disk theory faces significant challenges (e.g., Lawrence 2018). To calculate typical SS disk SEDs, we adopt a radiative efficiency of 10%, $\lambda_{Edd} = 0.1$, and an inner disk radius of the innermost stable circular orbit radius for a non-spinning BH. We vary M_{BH} to calculate the corresponding

---

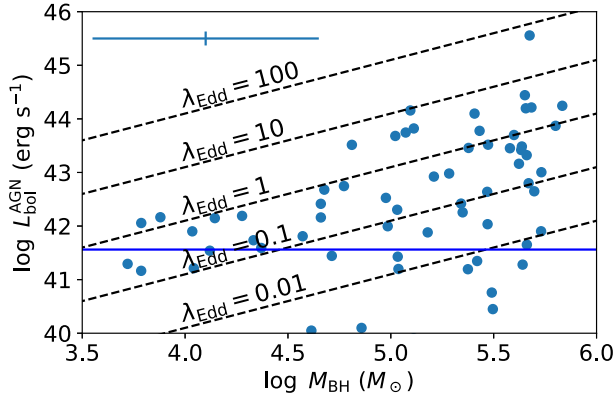[27] CIGALE adopts a temperature-independent disk SED model constructed based on SMBH AGNs.

Figure 16. M_{BH} vs. L_{bol}^{AGN} for our final sample. Typical error bars are presented in the upper-left corner. The error of M_{BH} is 0.55 dex, i.e., the scatter of the scaling relation in Reines & Volonteri (2015), compared to which the $M_\star$ uncertainty is negligible. The median error of L_{bol}^{AGN} is 0.13 dex, which is from the SED-fitting uncertainty and does not include possible systematic errors reported in Section 3.5. Several constant-λ_{Edd} lines are shown as the inclined dashed ones. The blue line presents a typical X-ray detection limit at our median redshift (0.2), assuming a typical k_{bol}^{AGN} value of 16.75. There are around 11 sources with very small L_{bol}^{AGN} ($<10^{40}$ erg s^{-1}) invisible in the figure, and their L_{bol}^{AGN} estimations are highly unreliable and underestimated.
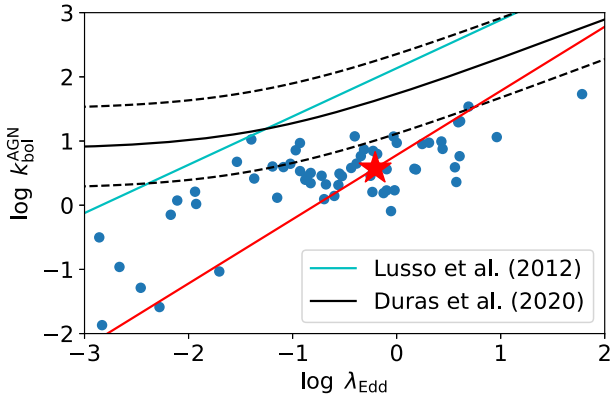
Figure 17. λ_{Edd} vs. k_{bol}^{AGN}. Sources with $\lambda_{Edd} \lesssim 0.1$ and unphysically small k_{bol}^{AGN} form a tail in the bottom-left corner and may have underestimated L_{bol}^{AGN}. The red star shows the median values among sources with $\lambda_{Edd} > 0.1$. The red line that has a slope of 1 and intersects with the red star denotes the trajectory when systematically shifting L_{bol}^{AGN}. The black lines represent the $\lambda_{Edd} - k_{bol}^{AGN}$ relation in Duras et al. (2020) and the corresponding 2σ deviations, and the cyan line is the type 1 relation in Lusso et al. (2012). Our sample significantly deviates from the expected relations.

SEDs. The results are shown in Figure 18, including five representative M_{BH} values: $10^9 M_\odot$ is the typical SMBH mass for Sloan Digital Sky Survey (SDSS) quasars (e.g., Shen et al. 2011), 10^6 and $10^2 M_\odot$ are our MBH mass range, $10^4 M_\odot$ is the middle point of the MBH mass range and also roughly the lower boundary of our estimated M_{BH} distribution (Figure 16), and $1 M_\odot$ represents a typical stellar-mass BH. The figure shows that the $10^9 M_\odot$ SMBH disk SED largely shows similar patterns as for the CIGALE AGN disk model adopted in Z22. Their deviations are not surprising because our illustrative model may be oversimplified, and it is known that the actual SMBH AGN disk SED differs from the SS disk SED (e.g., Davis & Laor 2011; Kubota & Done 2018). The disk SEDs of stellar-mass BHs are predicted to peak at X-rays, as known from XRBs. However, the MBH disk SEDs mainly peak in the EUV, where no direct data are available, though indirect probes

such as high-excitation emission lines may help us understand the EUV emission (e.g., Cann et al. 2018; Timlin & Brandt 2021). Also note that the disk emission of our sources is expected to contribute little to the X-rays, especially above 2 keV because our M_{BH} values ($\approx10^4$–$10^6 M_\odot$ with a median value of $2 \times 10^5 M_\odot$) are still much higher than those of stellar-mass BHs.

The MBH disk SEDs significantly deviate from the adopted AGN disk model in the SED fitting, which may cause strong biases. This problem is twofold. One is that the real MBH disk SED shape in the energy range covered by the data may be different, and the other is that the integrated L_{AGN}^{bol} may be wrong. The first problem can cause the fitting to fail and consequently affect the derived host-galaxy properties. Although we currently still lack good observational constraints on intrinsic MBH SEDs, Figure 18 indicates that in the IR-to-optical range, both SMBH and MBH disk SEDs have similar shapes in their low-energy tails. We thus suspect that the shape difference of the disk SED should not cause major problems to the SED-fitting quality and host-galaxy properties. The second problem, however, has the potential for causing trouble. Figure 18 shows that the normalized MBH disk SEDs are around 1 dex below the SMBH disk SEDs in the optical-to-IR range. A large fraction of disk emission may not be accounted for in our SED fitting, and inferring the missing part would inevitably rely on the assumed disk model to conduct extrapolations. Overall, this fundamental issue may lead to large underestimations of L_{AGN}^{bol}. Nevertheless, this issue may be mitigated when considering the dust emission, especially for type 2 AGNs, whose observed AGN SEDs should be mainly from their dust emission instead of the disk. The CIGALE SED model may still be applicable if the dust temperature does not vary much with M_{BH}, which is probably true because the dust temperature is bounded by dust sublimation.

We reiterate that our simple calculations are only for illustrative purposes and should not be taken as quantitative guidelines for correcting the bias. There are multiple factors not considered here. For example, more components besides the SS disk emission should be considered for more accurate SED calculations, and the model in Kubota & Done (2018) predicts more UV emission than for the SS disk; the accretion disk may evolve to a slim disk when λ_{Edd} increases (e.g., Abramowicz et al. 1988); it is unclear how the results would change after including the dust emission; the numerical underestimation factor should also depend on the adopted photometric bands; and even within our model, varying λ_{Edd} and inner disk radius, which depends on the BH spin, can also cause large shifts to the SEDs.

For the M_{BH} estimations, we used the empirical M_{BH}–$M_\star$ scaling relationship. Even though this is largely calibrated from massive galaxies, it may also hold for dwarf galaxies (e.g., Baldassare et al. 2020a), but possible biases may still exist (e.g., Reines & Volonteri 2015). Regardless of any possible systematic uncertainty of the relation itself, its large scatter (0.55 dex) is already notable. Our sample suffers from strong selection effects and thus may contain those objects with more massive MBHs so as to be detectable in X-rays. An example of a similar bias can be seen in Figure 18 of Burke et al. (2022), where their M_{BH} values of variability-selected active dwarf galaxies are 2–3 dex above the M_{BH}–$M_\star$ scaling relation. Similarly, Mezcua et al. (2023) also found a sample of distant active dwarf galaxies containing overmassive MBHs. It is
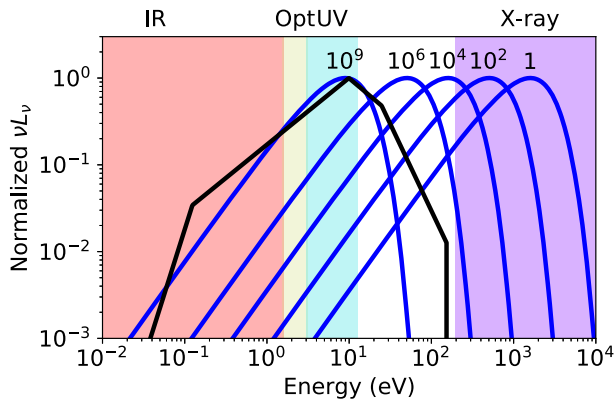
Figure 18. The blue curves show the predicted SS disk SEDs for different M_{BH}, as labeled in units of $M_\odot$ at the SED peaks. The black curve is the adopted disk SED in Z22. The SEDs are normalized such that the peak value is unity. The background shaded regions show the typical band ranges: IR (8000 Å–1000 μm, 10^{-3}–1.5 eV), optical (4000–8000 Å, 1.5–3 eV), UV (not including EUV; 1000–4000 Å, 3–12 eV), and X-ray (only showing the typical XMM-Newton energy range; 0.2–12 keV). The MBH disk SEDs may significantly deviate from the adopted CIGALE disk SED.

difficult to quantify the underlying bias given the overall limited knowledge about the dwarf population, but it should be noted that even a 2σ underestimation of M_{BH} is more than 1 dex and can largely mitigate the λ_{Edd} tension. In this case, our sources may actually contain more massive SMBHs instead of MBHs. Also, given that both L_{bol}^{AGN} and M_{BH} are likely to be underestimated, it is unclear if λ_{Edd} is underestimated or overestimated.

The $\lambda_{Edd} - k_{bol}^{AGN}$ relation is also largely uncertain in at least two respects. First, this relation was calibrated mainly based on AGNs with $\lambda_{Edd} \lesssim 1$, and thus extrapolations toward the super-Eddington regime are inevitable in Figure 17. The relations in Lusso et al. (2012) and Duras et al. (2020) also deviate from each other in the super-Eddington regime in Figure 17. Liu et al. (2021) found that candidate super-Eddington AGNs generally follow the same disk-corona correlation as for sub-Eddington AGNs, but their λ_{Edd} is still confined within 10. Given the aforementioned possible underestimations of L_{bol}^{AGN}, our sources may have larger λ_{Edd} beyond where there are good observational constraints, and thus the super-Eddington extrapolation is still uncertain. Second, the $\lambda_{Edd} - k_{bol}^{AGN}$ relation may be different for MBHs. It has been shown that the X-ray emission becomes relatively stronger with decreasing M_{BH} for SMBHs (e.g., Martocchia et al. 2017; Duras et al. 2020; Liu et al. 2021), and Desroches et al. (2009) and Dong et al. (2012) also found that type 1 active dwarf galaxies have higher ratios between their X-ray and UV emission compared to massive AGNs. Therefore, the real MBH $\lambda_{Edd} - k_{bol}^{AGN}$ relation may be lower than that for massive AGNs.

Overall, this section highlights the difficulties in measuring M_{BH}, L_{bol}^{AGN}, and consequently, λ_{Edd}, for active dwarf galaxies. The λ_{Edd} tension may be caused by many factors, and future work is needed to solve the challenges discussed in this section.

4. Summary

In this work, we searched for active dwarf galaxies in XMM-SERVS, and our main findings are summarized as follows:

1. After considering several contaminating factors, we found 73 active dwarf galaxies.

First, we highlight the importance of assessing the reliabilities of photo-zs and $M_\star$. Active dwarf galaxies present significant challenges for deriving reliable photo-zs, and the photo-zs of sources with high sSFR and/or $f_{AGN}(0.36$–4.5 μm; obs) may be unreliable. This difficulty does not only exist in our sample, but is also likely present in previous literature. It should also be checked if the SEDs are dominated by AGNs. In such a case, the returned $M_\star$ from SED fitting may be unreliable, causing the misidentifications of massive galaxies as dwarfs. These problems become prevalent with increasing redshift for flux-limited samples, and all of our active dwarf-galaxy candidates with $z > 1.1$ are found to be unreliable.

We further estimate the expected X-ray flux if a given dwarf of interest does not contain an AGN, including the XRB and hot gas emission that depend upon $M_\star$ and/or SFR. We found that given the XMM-Newton PSF aperture size, the flux from nearby sources usually dominates over the galaxy emission from the dwarf of interest itself. We require reliable active dwarf galaxies to have nonzero X-ray emission from their AGNs in a statistically significant manner. See Section 2.

2. Based on our new implementation of HR measurements, we obtained the HRs of our sources as indicators of the X-ray spectral shapes. Our HRs indicate that nearly none of our sources is heavily obscured, which contradicts the predictions based on massive-AGN XLFs. This may be because our sources have lower M_{BH} than SMBHs and hence higher λ_{Edd}, and the X-ray obscuration is fundamentally related to λ_{Edd} instead of L_X. The massive-AGN XLFs thus overestimate the obscuration for active dwarf galaxies. See Section 3.1.

3. We examined the radio properties of our sources. There are $\approx 1-5$ radio-excess AGNs and 28 non-radio-excess sources. This small radio-excess incidence is consistent with previous works. See Section 3.2.

4. We examined the host-galaxy environments of our sources. By measuring the projected separations on 100 kpc to $\gtrsim 1$ Mpc scales between dwarf galaxies and massive galaxies, we found that our sources have similar values with inactive dwarf galaxies after matching $M_\star$ and z, indicating that dwarf AGN activity generally may not be triggered by environmental effects. See Section 3.3.

5. We explored the AGN accretion distribution of dwarf galaxies, as quantified by $p(L_X|M_\star, z)$, after considering selection effects. A power-law formula with respect to $M_\star$, z, and L_X can provide good fits. The fitting results indicate that $p(L_X|M_\star, z)$ decreases with L_X and increases with $M_\star$, but redshift evolution cannot be statistically confirmed. $p(L_X|M_\star, z)$ can further be converted to the active fraction. Depending upon the exact AGN definition and $M_\star$ and z ranges, the active fraction is generally 10^{-5}–10^{-2}. As for $p(L_X|M_\star, z)$, the L_X-based active fraction increases with $M_\star$, but the λ_{sBHAR}-based active fraction shows much less significant $M_\star$ evolution. See Section 3.4.

6. We estimated L_{bol}^{AGN} from the SED fitting, M_{BH} from the M_{BH}–$M_\star$ scaling relation, and consequently, λ_{Edd}. However, our sources significantly deviate from the expected relation in the $\lambda_{Edd} - k_{bol}^{AGN}$ plane. We discuss possible underlying uncertainties of L_{bol}^{AGN}, M_{BH}, and the

$\lambda_{\rm Edd} - k_{\rm bol}^{\rm AGN}$ relation.

Especially, even $L_{\rm bol}^{\rm AGN}$, which is often considered robust, may suffer from strong biases inherent in the SED fitting. Our analyses raise the following questions that should be addressed in the future. How should one observationally constrain MBH SEDs? How large is the underlying bias when using SMBH AGN SED models to fit active dwarf galaxies? Do we need temperature-dependent AGN SED models, which currently have not been enabled in common SED-fitting tools? See Section 3.5.

Overall, our sample resides in a similar parameter space as the COSMOS sample in Mezcua et al. (2018) because of similar multiwavelength (especially X-ray) depths. Several of our sample's characteristics echo those of the COSMOS sample, including the limited fractions of high-HR sources and radio-excess AGNs, the smaller $\xi_{\rm AGN}^L$ compared to massive galaxies, and the high $\lambda_{\rm Edd}$, as summarized above. Our results on, e.g., photo-zs and selection effects also highlight some likely limitations of the COSMOS sample. Our sample is also $\approx$2–3 times larger.

Our 73 X-ray-selected active dwarf galaxies can serve as a useful sample beyond the local universe. It is important to further enrich the sample in the same fields. Especially, LSST will enable variability selection, and the variability timescale is also an indicator of $M_{\rm BH}$. The unreliable photo-z problem also causes strong selection biases and limits the sample size, and it may be necessary to obtain deep spectroscopic observations to measure spec-zs instead. Fortunately, several spectroscopic surveys will be available in our fields in the coming few years, as listed in Section 5 of Z22. Additionally, the X-ray sensitivity is the primary limitation for selecting more sources. Future missions such as STAR-X, AXIS, and Athena will push X-ray surveys on deg^2 scales deeper and thus can provide much larger active dwarf-galaxy samples.

Appendix A
Estimation of Hardness Ratio

Our method is based on the framework of Park et al. (2006) but with significant revisions and different algorithmic implementations. The main reasons for the revisions are to accelerate the computations and to implement the HR estimations in `Python` for the sake of convenience for `Python` users. For large X-ray surveys with thousands of sources, such as XMM-SERVS, a faster implementation than for Park et al. (2006) becomes notably helpful. As we will show in the following, the computation is accelerated by avoiding numerical integrations; instead, all the integrations can be solved analytically with some special functions involved. Furthermore, we found that numerical overflows sometimes happen in Park et al. (2006), but our method overcomes this problem.

Throughout this appendix, SB and HB are regarded as any two non-overlapping energy bands. We denote S and H as the total SB and HB counts in the source region, respectively, and they follow Poisson distributions:

$$S \sim {\rm Poi}(e_S(\lambda_S + \xi_S)), \quad H \sim {\rm Poi}(e_H(\lambda_H + \xi_H)), \quad {\rm (A1)}$$

where $e_\bullet$, $\lambda_\bullet$, and $\xi_\bullet$ are the exposure time, the true source count rate, and the expected background count rate in the source region, respectively. $e_\bullet$ is known from the observation, $\lambda_\bullet$ is unknown, and $\xi_\bullet$ is estimated from a background region. We assume that $\xi_\bullet$ is accurately known. This assumption is not adopted in Park et al. (2006) but is appropriate in most cases because the total counts in the background region are usually much larger than for the source region, given that the background area is generally much larger than the source region area. Besides, when this assumption fails, it is usually because the source is bright and many source counts are received. Such a case is even simpler—it is sufficiently accurate to adopt Gaussian errors and apply classic error propagation, and there is no need for Bayesian estimations. Another reason is that, for X-ray surveys that construct background maps to measure $\xi_\bullet$, there is not an accurate definition of background regions. Although we adopt this assumption in this work, it is not always necessary in general cases, and we will also present the method without this assumption in the last part of this appendix.

Following Park et al. (2006), the priors on λ_S and λ_H are assumed to be

$$\lambda_S \sim \gamma(\psi_{S1}, \psi_{S2}), \quad \lambda_H \sim \gamma(\psi_{H1}, \psi_{H2}), \quad {\rm (A2)}$$

where $\psi_\bullet$ are given in advance. The probability distribution function of $\gamma(\psi_1, \psi_2)$ is $\pi(x) = \psi_2^{\psi_1} x^{\psi_1-1} e^{-\psi_2 x} / \Gamma(\psi_1)$. This prior family includes several common noninformative priors: ($\psi_1 = 1$, $\psi_2 = 0$) is a flat prior in the linear scale, ($\psi_1 = 0.5$, $\psi_2 = 0$) is a Jeffrey prior, and ($\psi_1 \to 0^+$, $\psi_2 = 0$) is a flat prior in the logarithm scale.

The SB likelihood is

$$p(S|\lambda_S) = \frac{[e_S(\lambda_S + \xi_S)]^S e^{-e_S(\lambda_S + \xi_S)}}{S!}$$
$$= \frac{e_S^S e^{-e_S \xi_S}}{S!} \sum_{n=0}^{S} \binom{S}{n} \lambda_S^n \xi_S^{S-n} e^{-e_S \lambda_S}. \quad {\rm (A3)}$$

Therefore,

$$p(\lambda_S|S) \propto \pi(\lambda_S) p(S|\lambda_S) \propto \sum_{n=0}^{S} \binom{S}{n} \lambda_S^{n+\psi_{S1}-1} \xi_S^{S-n} e^{-(e_S+\psi_{S2})\lambda_S}. \quad {\rm (A4)}$$

Similarly, for the HB,

$$p(\lambda_H|H) \propto \sum_{m=0}^{H} \binom{H}{m} \lambda_H^{m+\psi_{H1}-1} \xi_H^{H-m} e^{-(e_H+\psi_{H2})\lambda_H}. \quad {\rm (A5)}$$

Under the assumption that the SB and the HB are independent, $p(\lambda_S, \lambda_H|S, H) = p(\lambda_S|S)p(\lambda_H|H)$. Denoting $w = \lambda_S + \lambda_H$, we can write $\lambda_S = (1 - HR)w/2$ and $\lambda_H = (1 + HR)w/2$. Thus, we have

$$p(HR, w|S, H) = \quad p(\lambda_S, \lambda_H|S, H)\left|\frac{\partial(\lambda_S, \lambda_H)}{\partial(HR, w)}\right|$$

$$= \frac{1}{2}wp\left(\lambda_S = \frac{(1-HR)w}{2}|S\right)p\left(\lambda_H = \frac{(1+HR)w}{2}|H\right). \quad (A6)$$

The HR posterior probability distribution function is

$$p(HR|S, H) = \int_0^{+\infty} p(HR, w|S, H)dw \quad (A7)$$

$$\propto \sum_{n=0}^{S}\sum_{m=0}^{H}\binom{S}{n}\binom{H}{m}\xi_S^{S-n}\xi_H^{H-m}2^{-(n+m+\psi_{S1}+\psi_{H1})}(1 - HR)^{n+\psi_{S1}-1}(1 + HR)^{m+\psi_{H1}-1}\times \quad (A8)$$

$$\int_0^{+\infty} w^{n+m+\psi_{S1}+\psi_{H1}-1}e^{-\frac{1}{2}[(e_S+\psi_{S2})(1-HR)+(e_H+\psi_{H2})(1+HR)]w}dw. \quad (A9)$$

Using the fact that $\int_0^{+\infty} w^a e^{-bw}dw = \Gamma(1 + a)\big/b^{1+a}$, the above equation can be expressed as follows:

$$p(HR|S, H) \propto \sum_{n=0}^{S}\sum_{m=0}^{H}\binom{S}{n}\binom{H}{m}\xi_S^{S-n}\xi_H^{H-m}\Gamma(n + m + \psi_{S1} + \psi_{H1})$$

$$\times \frac{(1 - HR)^{n+\psi_{S1}-1}(1 + HR)^{m+\psi_{H1}-1}}{[(e_S + \psi_{S2})(1 - HR) + (e_H + \psi_{H2})(1 + HR)]^{n+m+\psi_{S1}+\psi_{H1}}}. \quad (A10)$$

The HR posterior CDF is

$$F(HR|S, H) = \int_{-1}^{HR} p(HR = h|S, H)dh \quad (A11)$$

$$\propto \sum_{n=0}^{S}\sum_{m=0}^{H}\binom{S}{n}\binom{H}{m}\xi_S^{S-n}\xi_H^{H-m}\Gamma(n + m + \psi_{S1} + \psi_{H1})\times$$

$$\int_{-1}^{HR}\frac{(1-h)^{n+\psi_{S1}-1}(1+h)^{m+\psi_{H1}-1}}{[(e_S+\psi_{S2})(1-h)+(e_H+\psi_{H2})(1+h)]^{n+m+\psi_{S1}+\psi_{H1}}}dh. \quad (A12)$$

Denoting the integration as G and substituting $x = (1 + h)/2$, we have

$$G = \frac{1}{2}\frac{1}{(e_S + \psi_{S2})^{n+m+\psi_{S1}+\psi_{H1}}}\int_0^{\frac{1+HR}{2}}\frac{(1 - x)^{n+\psi_{S1}-1}x^{m+\psi_{H1}-1}}{\left[1 - \left(1 - \frac{e_H + \psi_{H2}}{e_S + \psi_{S2}}\right)x\right]^{n+m+\psi_{S1}+\psi_{H1}}}dx. \quad (A13)$$

The integration is of the form of $\int_0^b \frac{(1-x)^{z_1-1}x^{z_2-1}}{(1-ax)^{z_1+z_2}}dx$. We substitute $t = (1 - a)x/(1 - ax)$ and obtain

$$\int_0^b \frac{(1 - x)^{z_1-1}x^{z_2-1}}{(1 - ax)^{z_1+z_2}}dx = \frac{1}{(1 - a)^{z_2}}\int_0^{\frac{(1-a)b}{1-ab}}(1 - t)^{z_1-1}t^{z_2-1}dt = \frac{1}{(1 - a)^{z_2}}\frac{\Gamma(z_1)\Gamma(z_2)}{\Gamma(z_1 + z_2)}I_\beta\left(z_2, z_1; \frac{(1 - a)b}{1 - ab}\right), \quad (A14)$$

where I_β is the incomplete Beta function. Therefore,

$$G = \frac{\Gamma(n + \psi_{S1})\Gamma(m + \psi_{H1})}{2(e_S + \psi_{S2})^{n+\psi_{S1}}(e_H + \psi_{H2})^{m+\psi_{H1}}\Gamma(n + m + \psi_{S1} + \psi_{H1})}$$

$$\times I_\beta\left(m + \psi_{H1}, n + \psi_{S1}; \frac{(e_H + \psi_{H2})(1 + HR)}{(e_S + \psi_{S2})(1 - HR) + (e_H + \psi_{H2})(1 + HR)}\right). \quad (A15)$$

Substituting G into Equation (A12) we obtain

$$F(HR|S, H) \propto \sum_{n=0}^{S}\sum_{m=0}^{H}\binom{S}{n}\binom{H}{m}\xi_S^{S-n}\xi_H^{H-m}\Gamma(n + m + \psi_{S1} + \psi_{H1})G$$

$$\propto \sum_{n=0}^{S}\sum_{m=0}^{H}\Theta_{nm}(S, H, \xi_S, \xi_H)I_{nm}(y(HR, e_S, e_H)), \quad (A16)$$

$$\Theta_{nm}(S, H, \xi_S, \xi_H) = \frac{\Gamma(n + \psi_{S1})\Gamma(m + \psi_{H1})[(e_S + \psi_{S2})\xi_S]^{-n}[(e_H + \psi_{H2})\xi_H]^{-m}}{\Gamma(n + 1)\Gamma(m + 1)\Gamma(S - n + 1)\Gamma(H - m + 1)}, \quad (A17)$$

$$I_{nm}(y) = I_\beta(m + \psi_{H1}, n + \psi_{S1}; y),\qquad (A18)$$

$$y(\text{HR}, e_S, e_H) = \frac{(e_H + \psi_{H2})(1 + \text{HR})}{(e_S + \psi_{S2})(1 - \text{HR}) + (e_H + \psi_{H2})(1 + \text{HR})}. \qquad (A19)$$

The above equations return unnormalized $F(\text{HR}|S, H)$. The appropriate normalization such that $F(1|S, H) = 1$ is calculated by substituting $\text{HR} = 1$, and we obtain the normalized HR CDF as follows:

$$F(\text{HR}|S, H) = \frac{\sum\limits_{n=0}^{S}\sum\limits_{m=0}^{H} \Theta_{nm} I_{nm}}{\sum\limits_{n=0}^{S}\sum\limits_{m=0}^{H} \Theta_{nm}}. \qquad (A20)$$

Therefore, the HR CDF can be calculated without numerically conducting integrations. The CDF can then be easily converted to point estimators and confidence intervals. Furthermore, we notice that Θ_{nm} does not depend on HR and thus only needs to be computed once for each source. I_{nm} does not depend on (S, H, ξ_S, ξ_H), and its dependence on (e_S, e_H, HR) is all absorbed into the third parameter y of I_β in Equation (A18) given a set of (ψ_{S1}, ψ_{H1}), the possible values of the first and second parameters of I_β are countable. One can thus compute I_{nm} on a grid of y and (n, m) from 0 up to reasonably large values (e.g., 1000) and save the results externally; then I_{nm} does not need to be computed further when applying it to real sources. Note that I_{nm} can be computed quickly if only once using `scipy.special.betainc`. Therefore, one only needs to compute Θ_{nm} once per source and do the summations to obtain the full HR CDF on the chosen y grid, which can be converted to an HR grid. This implementation method allows fast and accurate HR estimations for a large number of sources. Practically, Θ_{nm} should be computed using a natural logarithm to avoid overflows (e.g., using `scipy.special.gammaln`).

In more general cases where $\xi_\bullet$ is not assumed to be accurately known, we need to estimate $\xi_\bullet$ from source-free background regions. We denote B_S and B_H as the SB and HB counts in the background region, respectively, and $r_\bullet$ as the ratio between the background region area and the source region area, where the term *area* here may include both the angular area and the sensitivity. That is, $B_S \sim \text{Poi}(r_S e_S \xi_S)$ and $B_H \sim \text{Poi}(r_H e_H \xi_H)$. Similar to Equation (A2), the priors on ξ_S and ξ_H are assumed to be

$$\xi_S \sim \gamma(\psi_{S3}, \psi_{S4}), \; \xi_H \sim \gamma(\psi_{H3}, \psi_{H4}). \qquad (A21)$$

Following the same procedures as above, except for an additional step to integrate out $\xi_\bullet$, we can prove that Equation (A20) still holds, and the only difference is on Θ_{nm}. Equation (A17) should be modified as follows:

We release `Python` codes implementing this algorithm at https://github.com/fanzou99/FastHR.

Appendix B
Detailed Analyses of XMM02399

Section 3.1 suggests that XMM02399 (R.A. = 02:21:56.53, decl.=−04:07:58.0, and SDSS spec-z = 0.615) is the only source in our sample with clear evidence of $N_H \gtrsim 10^{23}$ cm^{-2}. As far as we know, there has not been any Compton-thick (CT) active dwarf galaxy beyond the local universe confirmed yet. We thus analyze this candidate in detail in this appendix.

B.1. X-Ray Analyses

XMM02399 has been observed by XMM-Newton 6 times and by Chandra once. We list them as follows: XMM-Newton ObsIDs = 0037982201 (16.4 ks), 0404960601 (11.9 ks), 0785101501 (22.0 ks), 0785102001 (22.0 ks), 0793581001 (9.0 ks), 0793581301 (9.0 ks); Chandra ObsID = 20538 (9.9 ks). We reduce these observations and extract the corresponding spectra using the XMM-Newton Science Analysis System (SAS; v20.0) and the Chandra Interactive Analysis of Observations (CIAO; v4.12). We group these spectra to one count per bin. To help visualize the spectral fitting, we further merge all the XMM-Newton spectra into a single spectrum using the SAS task `epicspeccombine`. This merging procedure may produce slight biases, and thus we derive our numerical results by jointly fitting all the individual spectra instead of from the single merged spectrum.

We use `sherpa` to fit the X-ray spectra, in which the W statistic is adopted. We limit our spectral fitting range to 0.5–10 keV for XMM-Newton and 0.5–7 keV for Chandra and use the same model and parameters to fit all the spectra simultaneously. Using a simple power law absorbed by the Galactic absorption, to which we refer as the Pow model, we obtain a hard effective photon index of $-0.04^{+0.15}_{-0.16}$. To measure N_H, we phenomenologically adopt an absorbed power-law model. We also found the existence of an apparent scattered component below 2 keV, and hence we use another power law to account for this. We find no evidence indicating iron K lines and thus do not add them to the model. The resulting model, which will be called AbsPow, is `phabs×(zphabs×cabs×zpowerlw + constant×zpowerlw)`, where `phabs` models the Galactic absorption, the N_H values of `zphabs` and `cabs` are linked to account for the intrinsic obscuration, the two `zpowerlw` components are set to be the same, and `constant` describes the scattered fraction (f_{sc}). We obtain a nearly CT-level $N_H = 9.6^{+1.8}_{-1.6} \times 10^{23}$ cm^{-2} and a soft $\Gamma = 2.77^{+0.39}_{-0.37}$ with a good fit (W-stat/d.o.f. = 428/420). Physically, there should be reprocessed emission, and thus we try the following model: `phabs×(borus + zphabs×cabs×cutoffpl + constant×cutoffpl)`, where `borus` is the reprocessed torus emission model in Baloković et al. (2018). We refer to this model Torus hereafter. The N_H

$$\Theta_{nm} = \frac{\Gamma(S + B_S + \psi_{S3} - n)\Gamma(H + B_H + \psi_{H3} - m)\Gamma(n + \psi_{S1})\Gamma(m + \psi_{H1})}{\Gamma(n + 1)\Gamma(m + 1)\Gamma(S - n + 1)\Gamma(H - m + 1)}$$
$$\times \left[\frac{(1 + r_S)e_S + \psi_{S4}}{e_S + \psi_{S2}}\right]^n \left[\frac{(1 + r_H)e_H + \psi_{H4}}{e_H + \psi_{H2}}\right]^m. \qquad (A22)$$
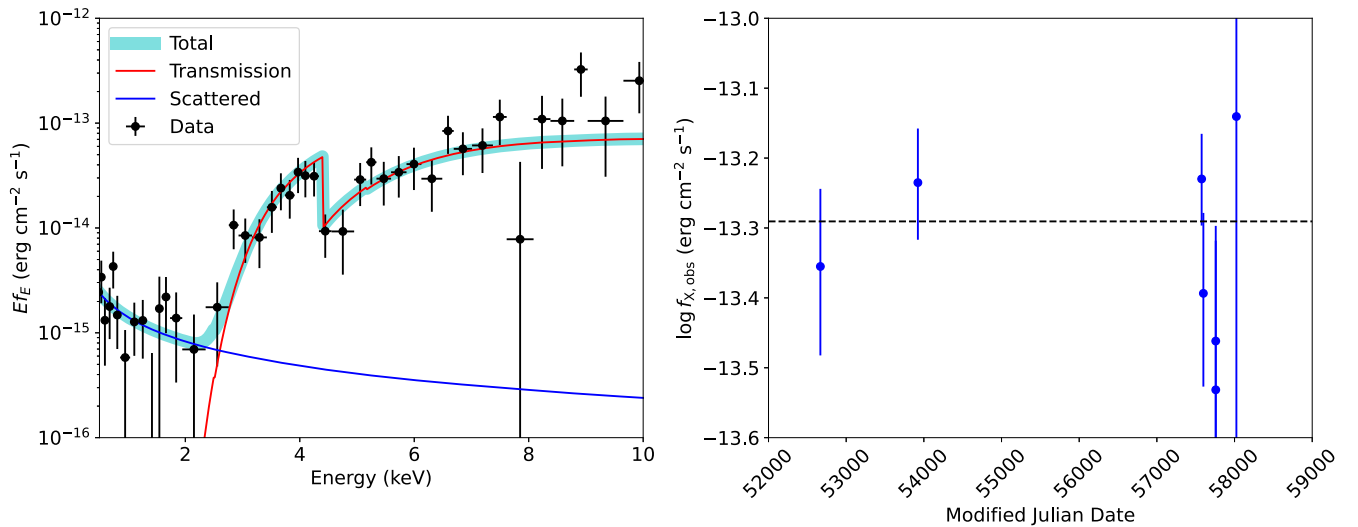
Figure 19. Left: the unfolded merged XMM-Newton spectrum (the points with error bars) fitted with the AbsPow model (the thick cyan curve). The model includes transmission and scattered components, as labeled by the legend. The spectrum is rebinned for visualization only, and this merged spectrum is presented only for illustration, while our scientific analyses are based on jointly fitting all the individual spectra. Right: $f_{\rm X,obs}$ vs. time. Each data point represents one X-ray observation. The horizontal black-dashed line marks our $f_{\rm X,obs}$ based on the original non-variable Pow model. No variability is visible for XMM02399.

Table 6
X-Ray Spectral Fitting Results of XMM02399

Model	W-stat/d.o.f.	Γ	$N_{\rm H}$ (cm^{-2})	$f_{\rm sc}$	$\log f_{\rm X}$ (erg cm^{-2} s^{-1})	$\log L_{\rm X}$ (erg s^{-1})
Pow	484/422	$-0.04^{+0.15}_{-0.16}$	$\cdots$	$\cdots$	$-13.29^{+0.05}_{-0.05}$	$43.50^{+0.03}_{-0.03}$
AbsPow	428/420	$2.77^{+0.39}_{-0.37}$	$9.6^{+1.8}_{-1.6} \times 10^{23}$	$1.4^{+2.2}_{-0.9} \times 10^{-3}$	$-12.22^{+0.24}_{-0.20}$	$45.12^{+0.34}_{-0.23}$
Torus	432/418	$2.60^{+u}_{-0.27}$	$9.5^{+1.8}_{-1.6} \times 10^{23}$	$2.2^{+2.6}_{-0.7} \times 10^{-3}$	$-12.32^{+0.19}_{-0.32}$	$45.01^{+0.19}_{-0.33}$

Note. $f_{\rm X}$ is the X-ray flux in the observed-frame 2–10 keV band, and $L_{\rm X}$ is the X-ray luminosity in the rest-frame 2–10 keV band. For the Pow model, the reported $f_{\rm X}$ and $L_{\rm X}$ are observed ones without absorption corrections, while the $f_{\rm X}$ and $L_{\rm X}$ of the AbsPow and Torus models are intrinsic ones. The results from the AbsPow model are adopted as the fiducial ones throughout this appendix.

values of borus, zphabs, and cabs are all set the same, and the cutoffpl parameters are linked to those of borus. The best-fit statistic is W-stat/d.o.f.=432/418, and the fitting returns $N_{\rm H} = 9.5^{+1.8}_{-1.6} \times 10^{23}$ cm^{-2} and $\Gamma = 2.60^{+u}_{-0.27}$, where $+u$ means that the best-fit Γ reaches the upper limit of the Γ domain, 1.4–2.6, allowed by the borus component. These results are similar to those from the AbsPow model. In fact, we found the reflection component in the best-fit Torus model is negligible, and thus the Torus model is effectively similar to the AbsPow model. Given the fact that the AbsPow model allows Γ to reach beyond 2.6 and provides a smaller best-fit statistic, we will adopt this model as our final one. We also refer to the observed flux ($f_{\rm X,obs}$) as the Pow result. We summarize our fitting results in Table 6. To visualize the spectrum, we show the Torus model fitting results in Figure 19. XMM02399 has a very high Γ value, which is rare and may indicate a high $\lambda_{\rm Edd}$ (see also Section 3.5 and Appendix B.4) because Γ is positively correlated with $\lambda_{\rm Edd}$ (e.g., Shemmer et al. 2008; Brightman et al. 2013). Sub-Eddington AGNs generally have $\Gamma \lesssim 2.2$, and even the Γ of reported super-Eddington AGN candidates ($1 \lesssim \lambda_{\rm Edd} \lesssim 10$) rarely exceeds 2.5 (e.g., Huang et al. 2020; Liu et al. 2021). Nevertheless, our Γ uncertainty is large, and thus the high Γ value is still statistically consistent with those of general AGNs.

The X-ray observations span a time range of 14 yr, which enables us to check if XMM02399 presents X-ray variability.

We first check if $f_{\rm X,obs}$ is variable. We use the Pow model to simultaneously fit all the observations, linking their Γ while allowing their normalizations to vary freely. Using a universal Γ reduces the number of parameters and helps improve the variability significance (if any). The resulting $f_{\rm X,obs}$ as a function of time is plotted in Figure 19, and no significant variability is visible. More rigorously, we compare the Bayesian information criteria (BIC) between the original Pow model (i.e., the normalizations are linked) and the variable Pow model (i.e., the normalizations are freed), and the latter has a much larger BIC than the former (differ by 30), which strongly disfavors the variable model because more free parameters are introduced while nearly not improving the fitting. Similarly, when using the AbsPow model, we always detect no variability, no matter if we free or link the Γ and $N_{\rm H}$ parameters. We thus conclude that XMM02399 is not a variable source in X-rays.

B.2. Optical Spectrum

XMM02399 was spectroscopically observed by SDSS. We show its spectrum in the left panel of Figure 20 after correcting the Galactic extinction based on the $E(B - V)$ map in Schlegel et al. (1998) and the extinction law in Cardelli et al. (1989). We explicitly mark emission lines identified through visual inspection and matching wavelengths with those in Vanden
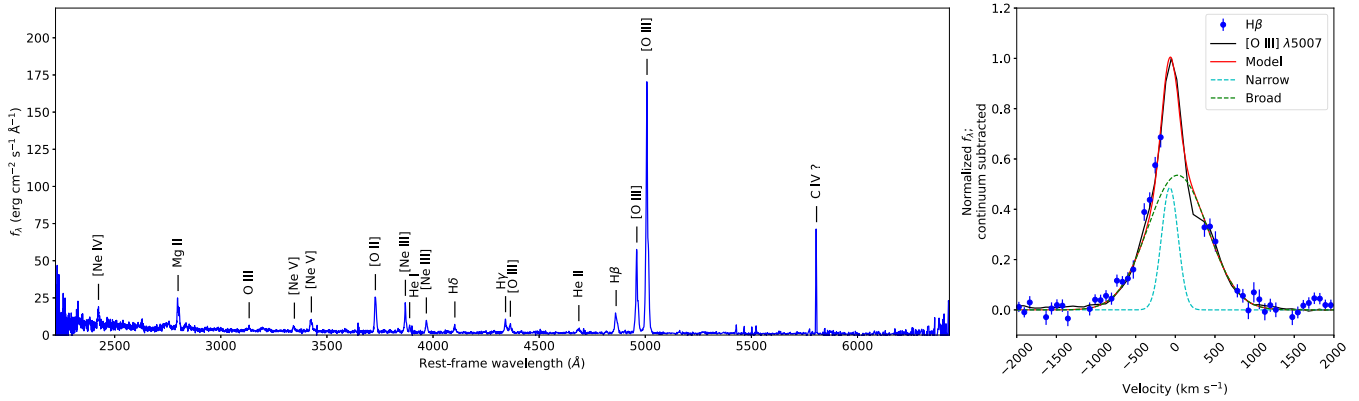
Figure 20. Left: SDSS rest-frame spectrum of XMM02399 after correcting for Galactic extinction. Apparent emission lines are marked explicitly. The C IV λ5808 line is uncertain due to large uncertainties in the corresponding pixels. Right: normalized Hβ and [O III] λ5007 profiles in the velocity space. Negative velocity indicates blueshift. Hβ is shown as points with error bars, while [O III] λ5007 is shown as the black solid line. The best-fit model for [O III] λ5007 is shown as the red solid line, whose narrow and broad components are plotted as the cyan and green-dashed lines, respectively. Hβ is consistent with the [O III] λ5007 profile.

Berk et al. (2001). There is a visually strong C IV λ5808 line, but the corresponding pixel errors are large, and thus its existence is uncertain. The velocity shifts of these emission lines (e.g., Mg II, [O II], and [O III]) relative to each other and the SDSS pipeline spec-z are generally a few tens of kilometers per second, and such small shifts are within intrinsic uncertainties of their systemic redshifts (e.g., Shen et al. 2016).

Several high-ionization lines are present, including the [Ne V] and He II λ4686 lines, which require ionizing photon energies above 97.1 and 54.4 eV, respectively. They cannot be explained by normal stellar populations. To examine the general excitation mechanism, we rely on the emission-line diagnostics in Lamareille (2010) and Juneau et al. (2014), where the former uses [O III] λ5007/Hβ versus [O II] λ3727/Hβ, and the latter uses [O III] λ5007/Hβ versus $M_\star$. To model these emission lines, we fit the continuum locally with a power law. [O II] λ3727 is then fitted using a narrow Gaussian line. [O III] λ5007 and Hβ are fitted together with [O III] λ4959, and each of them is fitted with two Gaussian lines to represent a narrow component and a broad component (see the next paragraph). We then measure their narrow-component equivalent widths to calculate the line ratios and obtain [O III] λ5007/Hβ = 8.3 and [O II] λ3727/Hβ = 3.0. These place our source into the AGN locus under both criteria in Lamareille (2010) and Juneau et al. (2014). Therefore, the primary excitation source of these lines is the AGN.

We further check its Mg II and Hβ lines. Mg II can be explained by two narrow components accounting for its doublet nature. For Hβ, we show its normalized profile together with [O III] λ5007 in the right panel of Figure 20. The [O III] λ5007 profile has a narrow core and a broad component, and the broad component is expected to be from outflows and has an FWHM of 891 km s^{-1}. The Hβ data points are in perfect consistency with the [O III] λ5007 profile. Several Hβ data points are missing around its peak because they fail the SDSS `and_mask`, but they are also consistent with the [O III] λ5007 profile if added. Similarly, Hβ is also consistent with the [O III] λ4959 profile. These similarities in line profiles are generally not expected if the broad Hβ component is from the broad-line region (e.g., Zou et al. 2020), and we hence suspect that Hβ is also broadened by outflows. Therefore, XMM02399 is actually a narrow-line AGN in terms of its optical spectrum.

B.3. SED and $M_\star$

We revise the bulk SED fitting in Z22 for XMM02399. There are three main reasons that the SED fitting can be improved. First, CIGALE requires the input X-ray photometry to be de-absorbed. The empirical X-ray absorption correction in Z22 is not appropriate for Compton-thick AGNs, and we will instead update the X-ray photometry using our results in Appendix B.1. Second, the strong [O III] λ4959 and [O III] λ5007 lines, as can be clearly seen in Figure 20 and 21, contaminate the i-band photometry. CIGALE is currently incapable of fitting AGN-produced emission lines (but it can fit emission lines from H II regions; e.g., Villa-Vélez et al. 2021), and thus we exclude the i-band photometry in the SED. Third, the reported sSFR of our source in Z22 is $10^{-7.67}$ yr^{-1}, almost reaching the maximum sSFR allowed by the normal-galaxy SFH in Z22. This indicates that the SFH of XMM02399 may need to be revised to a bursting one, and we will use the BQ SFH in Z22. The first two problems actually do not have substantial impacts on $M_\star$, but the third problem regarding its SFH is notable. We apply all three changes and show the best-fit SED and SFH, together with the original ones in Z22, in Figure 21. Their best-fit SFHs are significantly different—the Z22 SFH only includes a young stellar population, while our revised SFH includes a strong old stellar population and a very young bursting population. Consequently, the revised SED fitting returns a much larger $M_\star$—the Z22 (best fit and likelihood weighted) $M_\star = 2 \times 10^9 \, M_\odot$, while the revised best-fit $M_\star = 4 \times 10^{10} \, M_\odot$, and the revised likelihood-weighted $M_\star = 8 \times 10^9 \, M_\odot$.

The SEDs reveal that two main underlying uncertainties undermine $M_\star$ measurements. First, both best-fit SEDs in Figure 21 indicate that the galaxy component dominates below rest frame ~0.8 μm, and the AGN component dominates above rest frame ~2.2 μm, but the relative AGN contribution to the part between rest frame ~0.8 and 2.2 μm is unclear. The VIDEO H and K_s bands reside in this wavelength range, and SED models with either significant or negligible AGN contributions to these two bands can return reasonably good results. However, this wavelength range is where the old stellar emission peaks, and thus the AGN contamination prevents us from constraining the old stellar emission. Second, XMM02399 is a strong starburst galaxy, in which old stars may also be outshined by recently formed young stars, and thus
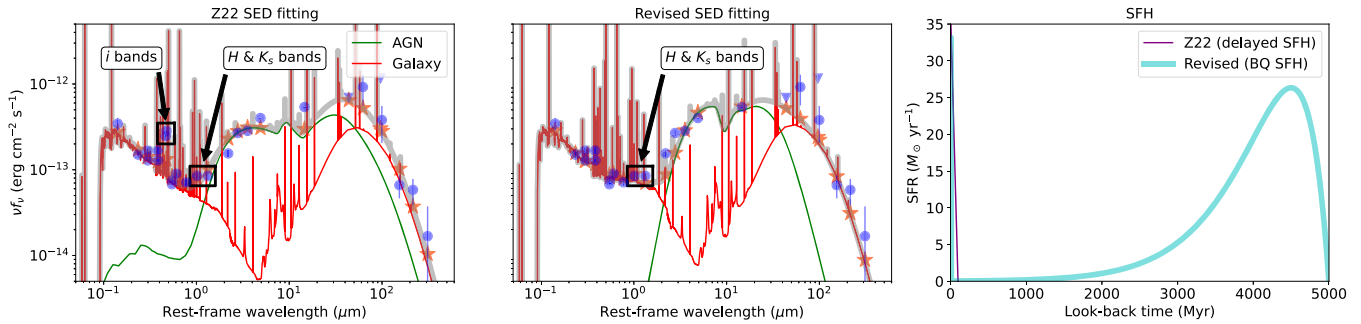
Figure 21. The best-fit SEDs of XMM02399 in Z22 (left) and this appendix (middle) and the corresponding SFHs (right). These SEDs are plotted in the same manner as in Figure 3, and their abscissa axes are truncated in the UV to help focus on their differences in the IR. The i bands, which are contaminated by strong [O III] lines, are marked explicitly in the left panel and excluded in our revised SED fitting. The H and K_s bands are also marked to highlight the different explanations of their origins in the two different SED models—the galaxy component dominates in the H and K_s bands in the middle panel but not in the left panel.

the SED-fitted $M_\star$ strongly depends upon how many old stars are allowed in the adopted SFH. When using galaxy-only models, the delayed SFH and BQ SFH return very different $M_\star$ by up to 1 dex. In fact, the second problem is aggravated by the first one—it is necessary to obtain the amount of galaxy emission at $\sim 1\,\mu$m to constrain the old stellar emission, but this becomes infeasible given our data because of plausible AGN contamination.

Therefore, the real $M_\star$ is upper bounded by the extreme case that the rest frame ~ 0.8–$2.2\,\mu$m is dominated by the galaxy component, and many old stars exist; similarly, $M_\star$ is lower bounded in the conversely extreme case. The revised best-fit SED (middle panel in Figure 21) happens to be the first extreme case, and the Z22 result corresponds to the second. Therefore, the real $M_\star$ should be roughly between 2×10^9 and $4 \times 10^{10}\,M_\odot$ (the statistical uncertainties are much smaller than these systematic uncertainties). Any value between this range is possible, which explains why the revised likelihood-weighted $M_\star$ is much smaller than the revised best-fit $M_\star$. Therefore, XMM02399 is still a low-mass galaxy candidate, but we cannot determine its actual $M_\star$. To further narrow the plausible $M_\star$ range, it is essential to directly constrain its galaxy and AGN contribution at rest-frame ~ 0.8–$2.2\,\mu$m (i.e., observed-frame ~ 1.3–$3.5\,\mu$m). Hubble or JWST IR imaging should be able to spatially resolve the galaxy and AGN components, as done for SDSS quasars (e.g., Li et al. 2021).

We note that the problem discussed in this appendix is not prevalent in our whole sample. XMM02399 happens to be the most extreme case in several respects (e.g., high N_H and sSFR). The last paragraph of Section 2.1.2 indicates that XMM02399 is the only source with $M_\star^{\text{bqgal}} > 10^{10}\,M_\odot$, and our other sources generally have much more reliable $M_\star$.

B.4. Further Discussion

Regardless of the $M_\star$ uncertainty, XMM02399 is an interesting object. Its several properties are the same as the high-λ_{Edd} dust-obscured galaxy (DOG) population in Zou et al. (2020): heavy obscuration in X-rays, moderate [O III] outflow (FWHM $\lesssim 1000\,\text{km s}^{-1}$), and starburst host galaxy. This may indicate that XMM02399 is physically at the same evolutionary stage with high-λ_{Edd} DOGs, i.e., at the peak of both BH and galaxy growth in a merger-driven event (see Section 5.1 of Zou et al. 2020 for further discussion).

If XMM02399 is indeed similar to high-λ_{Edd} DOGs, it should lie around the boundary between the allowed and

forbidden regions in the $\lambda_{\text{Edd}} - N_H$ plane (e.g., Ishibashi et al. 2018; Figure 7 of Zou et al. 2020), and this boundary returns $\lambda_{\text{Edd}} \approx 1$ at our N_H in Appendix B.1. Independently, its soft Γ also indicates that its λ_{Edd} may be high, and we obtain $\lambda_{\text{Edd}} = 11$ using the super-Eddington $\Gamma - \lambda_{\text{Edd}}$ relation in Huang et al. (2020). As another approach, following Section 3.5, we use the $M_\star$ range in Appendix B.3 to estimate the λ_{Edd} range and obtain λ_{Edd} to be between 3 and 71. These λ_{Edd} estimations are crude, but all lead to the same conclusion that XMM02399 is an Eddington-limited AGN with λ_{Edd} between unity and a few tens.

ORCID iDs

Fan Zou ⓘ https://orcid.org/0000-0002-4436-6923
W. N. Brandt ⓘ https://orcid.org/0000-0002-0167-2453
Qingling Ni ⓘ https://orcid.org/0000-0002-8577-2717
Shifu Zhu ⓘ https://orcid.org/0000-0002-1653-4969
David M. Alexander ⓘ https://orcid.org/0000-0002-5896-6313
Franz E. Bauer ⓘ https://orcid.org/0000-0002-8686-8737
Chien-Ting J. Chen ⓘ https://orcid.org/0000-0002-4945-5079
Bin Luo ⓘ https://orcid.org/0000-0002-9036-0063
Mouyuan Sun ⓘ https://orcid.org/0000-0002-0771-2153
Cristian Vignali ⓘ https://orcid.org/0000-0002-8853-9611
Fabio Vito ⓘ https://orcid.org/0000-0003-0680-9305
Yongquan Xue ⓘ https://orcid.org/0000-0002-1935-8104
Wei Yan ⓘ https://orcid.org/0000-0001-9519-1812

References

Abramowicz, M. A., Czerny, B., Lasota, J. P., & Szuszkiewicz, E. 1988, ApJ, 332, 646
Aird, J., Coil, A. L., & Georgakakis, A. 2018, MNRAS, 474, 1225
Aird, J., Coil, A. L., Moustakas, J., et al. 2012, ApJ, 746, 90
Ansh, S., Chen, C.-T. J., Brandt, W. N., et al. 2023, ApJ, 942, 82
Baldassare, V. F., Dickey, C., Geha, M., & Reines, A. E. 2020a, ApJL, 898, L3
Baldassare, V. F., Geha, M., & Greene, J. 2018, ApJ, 868, 152
Baldassare, V. F., Geha, M., & Greene, J. 2020b, ApJ, 896, 10
Baloković, M., Brightman, M., Harrison, F. A., et al. 2018, ApJ, 854, 42
Barai, P., & de Gouveia Dal Pino, E. M. 2019, MNRAS, 487, 5549
Barlow, R. 1990, NIMPA, 297, 496
Basu-Zych, A. R., Hornschemeier, A. E., Haberl, F., et al. 2020, MNRAS, 498, 1651
Bernstein, G. M., Trilling, D. E., Allen, R. L., et al. 2004, AJ, 128, 1364
Betancourt, M. 2017, arXiv:1701.02434
Birchall, K. L., Watson, M. G., & Aird, J. 2020, MNRAS, 492, 2268
Birchall, K. L., Watson, M. G., Aird, J., & Starling, R. L. C. 2022, MNRAS, 510, 4556
Bonzini, M., Padovani, P., Mainieri, V., et al. 2013, MNRAS, 436, 3759

Brammer, G. B., van Dokkum, P. G., & Coppi, P. 2008, ApJ, 686, 1503
Brandt, W. N., & Yang, G. 2022, in Handbook of X-ray and Gamma-ray Astrophysics, ed. C. Bambo & A. Santangelo (Singapore: Springer), 78
Brightman, M., Silverman, J. D., Mainieri, V., et al. 2013, MNRAS, 433, 2485
Burke, C. J., Liu, X., Shen, Y., et al. 2022, MNRAS, 516, 2736
Burke, C. J., Shen, Y., Liu, X., et al. 2023, MNRAS, 518, 1880
Calabrò, A., Amorín, R., Fontana, A., et al. 2017, A&A, 601, A95
Cann, J. M., Satyapal, S., Abel, N. P., et al. 2018, ApJ, 861, 142
Cardelli, J. A., Clayton, G. C., & Mathis, J. S. 1989, ApJ, 345, 245
Chabrier, G. 2003, PASP, 115, 763
Chen, C.-T. J., Brandt, W. N., Luo, B., et al. 2018, MNRAS, 478, 2132
Civano, F., Marchesi, S., Comastri, A., et al. 2016, ApJ, 819, 62
Condon, J. J. 1992, ARA&A, 30, 575
Conroy, C. 2013, ARA&A, 51, 393
Curti, M., Mannucci, F., Cresci, G., & Maiolino, R. 2020, MNRAS, 491, 944
Davis, F., Kaviraj, S., Hardcastle, M. J., et al. 2022, MNRAS, 511, 4109
Davis, S. W., & Laor, A. 2011, ApJ, 728, 98
Desroches, L.-B., Greene, J. E., & Ho, L. C. 2009, ApJ, 698, 1515
Doe, S., Nguyen, D., Stawarz, C., et al. 2007, in ASP Conf. Ser. 376, Astronomical Data Analysis Software and Systems XVI, ed. R. A. Shaw, F. Hill, & D. J. Bell (San Francisco, CA: ASP), 543
Dong, R., Greene, J. E., & Ho, L. C. 2012, ApJ, 761, 73
Duras, F., Bongiorno, A., Ricci, F., et al. 2020, A&A, 636, A73
Farrell, S. A., Webb, N. A., Barret, D., Godet, O., & Rodrigues, J. M. 2009, Natur, 460, 73
Fragos, T., Lehmer, B. D., Naoz, S., Zezas, A., & Basu-Zych, A. 2013, ApJL, 776, L31
Franzen, T. M. O., Banfield, J. K., Hales, C. A., et al. 2015, MNRAS, 453, 4020
Freeman, P., Doe, S., & Siemiginowska, A. 2001, Proc. SPIE, 4477, 76
Gallazzi, A., Charlot, S., Brinchmann, J., White, S. D. M., & Tremonti, C. A. 2005, MNRAS, 362, 41
Georgakakis, A., Nandra, K., Laird, E. S., Aird, J., & Trichas, M. 2008, MNRAS, 388, 1205
Greene, J. E., Strader, J., & Ho, L. C. 2020, ARA&A, 58, 257
Gültekin, K., King, A. L., Cackett, E. M., et al. 2019, ApJ, 871, 80
Gültekin, K., Nyland, K., Gray, N., et al. 2022, MNRAS, 516, 6123
Heywood, I., Hale, C. L., Jarvis, M. J., et al. 2020, MNRAS, 496, 3469
Heywood, I., Jarvis, M. J., Hale, C. L., et al. 2022, MNRAS, 509, 2150
Huang, J., Luo, B., Du, P., et al. 2020, ApJ, 895, 114
Ibar, E., Cirasuolo, M., Ivison, R., et al. 2008, MNRAS, 386, 953
Illingworth, G., Magee, D., Bouwens, R., et al. 2016, arXiv:1606.00841
Inayoshi, K., Visbal, E., & Haiman, Z. 2020, ARA&A, 58, 27
Ishibashi, W., Fabian, A. C., Ricci, C., & Celotti, A. 2018, MNRAS, 479, 3335
Jarvis, M. J., Bonfield, D. G., Bruce, V. A., et al. 2013, MNRAS, 428, 1281
Juneau, S., Bournaud, F., Charlot, S., et al. 2014, ApJ, 788, 88
Kellermann, K. I., Sramek, R., Schmidt, M., Shaffer, D. B., & Green, R. 1989, AJ, 98, 1195
Kim, D.-W., & Fabbiano, G. 2015, ApJ, 812, 127
Kormendy, J., & Ho, L. C. 2013, ARA&A, 51, 511
Koudmani, S., Sijacki, D., Bourne, M. A., & Smith, M. C. 2019, MNRAS, 484, 2047
Kroupa, P. 2001, MNRAS, 322, 231
Kubota, A., & Done, C. 2018, MNRAS, 480, 1247
Laigle, C., McCracken, H. J., Ilbert, O., et al. 2016, ApJS, 224, 24
Lamareille, F. 2010, A&A, 509, A53
Latimer, L. J., Reines, A. E., Bogdan, A., & Kraft, R. 2021, ApJL, 922, L40
Lawrence, A. 2018, NatAs, 2, 102
Lehmer, B. D., Basu-Zych, A. R., Mineo, S., et al. 2016, ApJ, 825, 7
Lehmer, B. D., Berkeley, M., Zezas, A., et al. 2014, ApJ, 789, 52
Lehmer, B. D., Eufrasio, R. T., Basu-Zych, A., et al. 2021, ApJ, 907, 17
Leja, J., Johnson, B. D., Conroy, C., et al. 2019, ApJ, 877, 140
Li, J., Xue, Y., Sun, M., et al. 2019, ApJ, 877, 5
Li, J. I. H., Shen, Y., Ho, L. C., et al. 2021, ApJ, 906, 103
Liu, H., Luo, B., Brandt, W. N., et al. 2021, ApJ, 910, 103
Liu, T., Tozzi, P., Wang, J.-X., et al. 2017, ApJS, 232, 8
Loredo, T. J. 2004, in AIP Conf. Proc. 735, 24th Int. Workshop on Bayesian Inference and Maximum Entropy Methods in Science and Engineering, ed. R. Fischer, R. Preuss, & U. V. Toussaint (Melville, NY: AIP), 195

Luo, B., Brandt, W. N., Xue, Y. Q., et al. 2017, ApJS, 228, 2
Lupi, A., Sbarrato, T., & Carniani, S. 2020, MNRAS, 492, 2528
Lusso, E., Comastri, A., Simmons, B. D., et al. 2012, MNRAS, 425, 623
LSST Science Collaboration, Abell, P. A., Allison, J., et al. 2009, arXiv:0912.0201
Madau, P., & Dickinson, M. 2014, ARA&A, 52, 415
Manzano-King, C. M., Canalizo, G., & Sales, L. V. 2019, ApJ, 884, 54
Marchesi, S., Civano, F., Elvis, M., et al. 2016, ApJ, 817, 34
Martocchia, S., Piconcelli, E., Zappacosta, L., et al. 2017, A&A, 608, A51
Merloni, A., Bongiorno, A., Brusa, M., et al. 2014, MNRAS, 437, 3550
Mezcua, M. 2017, IJMPD, 26, 1730021
Mezcua, M., Civano, F., Fabbiano, G., Miyaji, T., & Marchesi, S. 2016, ApJ, 817, 20
Mezcua, M., Civano, F., Marchesi, S., et al. 2018, MNRAS, 478, 2576
Mezcua, M., Siudek, M., Suh, H., et al. 2023, ApJL, 943, L5
Mezcua, M., Suh, H., & Civano, F. 2019, MNRAS, 488, 685
Mineo, S., Gilfanov, M., & Sunyaev, R. 2012, MNRAS, 426, 1870
Ng, E. W., & Geller, M. 1969, JRNBB, 73, 1
Ni, Q., Brandt, W. N., Chen, C.-T., et al. 2021, ApJS, 256, 21
Ni, Q., Timlin, J., Brandt, W. N., & Yang, G. 2019, RNAAS, 3, 5
Nyland, K., Lacy, M., Brandt, W. N., et al. 2023, RNAAS, 7, 33
Pacifici, C., Iyer, K. G., Mobasher, B., et al. 2023, ApJ, 944, 141
Papovich, C., Dickinson, M., & Ferguson, H. C. 2001, ApJ, 559, 620
Pardo, K., Goulding, A. D., Greene, J. E., et al. 2016, ApJ, 831, 203
Park, T., Kashyap, V. L., Siemiginowska, A., et al. 2006, ApJ, 652, 610
Paulino-Afonso, A., Sobral, D., Darvish, B., et al. 2020, A&A, 633, A70
Penny, S. J., Masters, K. L., Smethurst, R., et al. 2018, MNRAS, 476, 979
Pozzetti, L., Bolzonella, M., Zucca, E., et al. 2010, A&A, 523, A13
Prestwich, A. H., Tsantaki, M., Zezas, A., et al. 2013, ApJ, 769, 92
Read, A. M., Rosen, S. R., Saxton, R. D., & Ramirez, J. 2011, A&A, 534, A34
Reines, A. E. 2022, NatAs, 6, 26
Reines, A. E., Greene, J. E., & Geha, M. 2013, ApJ, 775, 116
Reines, A. E., & Volonteri, M. 2015, ApJ, 813, 82
Ricci, C., Trakhtenbrot, B., Koss, M. J., et al. 2017, Natur, 549, 488
Robitaille, T., Deil, C., & Ginsburg, A. 2020, reproject: Python-based astronomical image reprojection, Astrophysics Source Code Library, ascl:2011.023
Salpeter, E. E. 1955, ApJ, 121, 161
Schlegel, D. J., Finkbeiner, D. P., & Davis, M. 1998, ApJ, 500, 525
Schramm, M., Silverman, J. D., Greene, J. E., et al. 2013, ApJ, 773, 150
Shakura, N. I., & Sunyaev, R. A. 1973, A&A, 24, 337
Shemmer, O., Brandt, W. N., Netzer, H., Maiolino, R., & Kaspi, S. 2008, ApJ, 682, 81
Shen, Y., Brandt, W. N., Richards, G. T., et al. 2016, ApJ, 831, 7
Shen, Y., Richards, G. T., Strauss, M. A., et al. 2011, ApJS, 194, 45
Siudek, M., Mezcua, M., & Krywult, J. 2023, MNRAS, 518, 724
Speagle, J. S., Steinhardt, C. L., Capak, P. L., & Silverman, J. D. 2014, ApJS, 214, 15
Timlin, J. D. I., Brandt, W. N., & Laor, A. 2021, MNRAS, 504, 5556
Tumlinson, J., Peeples, M. S., & Werk, J. K. 2017, ARA&A, 55, 389
Ueda, Y., Akiyama, M., Hasinger, G., Miyaji, T., & Watson, M. G. 2014, ApJ, 786, 104
van der Wel, A., Bell, E. F., Häussler, B., et al. 2012, ApJS, 203, 24
Vanden Berk, D. E., Richards, G. T., Bauer, A., et al. 2001, AJ, 122, 549
Villa-Vélez, J. A., Buat, V., Theulé, P., Boquien, M., & Burgarella, D. 2021, A&A, 654, A153
Ward, C., Gezari, S., Nugent, P., et al. 2022, ApJ, 936, 104
Whitaker, K. E., Ashas, M., Illingworth, G., et al. 2019, ApJS, 244, 16
Yang, G., Boquien, M., Brandt, W. N., et al. 2022, ApJ, 927, 192
Yang, G., Brandt, W. N., Darvish, B., et al. 2018a, MNRAS, 480, 1022
Yang, G., Brandt, W. N., Vito, F., et al. 2018b, MNRAS, 475, 1887
Zhu, S. F., Brandt, W. N., Luo, B., et al. 2020, MNRAS, 496, 245
Zhu, S. F., Brandt, W. N., Zou, F., et al. 2023, MNRAS, 522, 3506
Zou, F., Brandt, W. N., Chen, C.-T., et al. 2022, ApJS, 262, 15
Zou, F., Brandt, W. N., Lacy, M., et al. 2021a, RNAAS, 5, 31
Zou, F., Brandt, W. N., Vito, F., et al. 2020, MNRAS, 499, 1823
Zou, F., Yang, G., Brandt, W. N., et al. 2021b, RNAAS, 5, 56